ScientificScholar®
Knowledge is power
Publisher of Scientific Journals

https://arabjchem.org

Arabian Journal of Chemistry

2025 18 (4) 762024

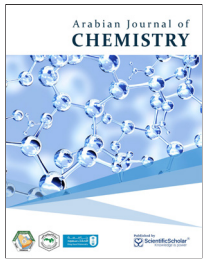

Original Article

Neuroprotective effects of intranasal mPEG-PLA modified nanoliposomes loaded with Gleditsiae Fructus Abnormalis volatile on cerebral ischemia-reperfusion injury *via* the HIF-1α/VEGF signaling pathway

Wenyuan Chen[a,b], Linli Jiang[a], Lei Chen[a], Nana Dong[c], Lan Qin[a], Yixue Lin[a], Yong Gao[a], Zhigang Ju[a], Yuxin Pang[a], Xiaolan Chen[a,*]

[a]*School of Pharmacy, Guizhou University of Traditional Chinese Medicine, Guiyang 550025, Guizhou, China*
[b]*School of Pharmacy, Bijie Medical College, Bijie, 551700, Guizhou, China*
[c]*Department of Pharmacy, Hospital of Traditional Chinese Medicine of Yuping Dong Autonomous County, Yuping, Tongren, China*

ARTICLE INFO

Keywords:
Cerebral ischemia-reperfusion injury
Gleditsiae Fructus Abnormalis
HIF-1α
Intranasal drug delivery
mPEG-PLA nanoliposomes
VEGF

ABSTRACT

Sustained release of neuroprotective agents from polymeric nanocarriers offers a promising approach for ischemic stroke treatment. This study investigates the neuroprotective effects of methoxy poly(ethylene glycol)-poly(lactic acid) (mPEG-PLA) modified nanoliposomes (mLP) loaded with Gleditsiae Fructus Abnormalis volatile oil (VOGFA) on cerebral ischemia-reperfusion injury (CIRI) in rats. Five active components—paeonol, eugenol, methyl eugenol, linalool, and anethole—were identified and screened for their potential to mitigate ischemic damage. The five active components of VOGFA of mPEG-PLA modified nanoliposomes (FVOGFA-mLP) system was prepared using an optimized ethanol injection method and characterized using transmission electron microscopy (TEM) and laser granulometry to evaluate particle size distribution and encapsulation efficiency. *In vitro* studies on PC12 cells subjected to oxygen-glucose deprivation/reperfusion (OGD/R) demonstrated that FVOGFA-mLP significantly enhanced cell survival and migration. *In vivo* experiments further confirmed the improved brain targeting capability and bioavailability of FVOGFA-mLP, which significantly reduced inflammatory cytokine levels [tumor necrosis factor-alpha (TNF-α), interleukin-6 (IL-6), and interleukin-1 beta (IL-1β)] and upregulated VEGF expression in cortical regions of CIRI rats. Behavioral assessments and histological analysis showed that medium and high doses of FVOGFA-mLP notably improved neurological function and reduced infarct volume, outperforming nimodipine. This study highlights the therapeutic potential of FVOGFA-mLP for ischemic stroke, demonstrating enhanced brain targeting and neuroprotection through the regulation of hypoxia-inducible factor 1-alpha (HIF-α) and vascular endothelial growth factor (VEGF) signaling pathways.

1. Introduction

Ischemic stroke has become the second leading cause of death and a primary cause of disability worldwide [1]. It results from insufficient blood supply to the brain, leading to necrosis of brain tissue [2]. Studies indicate that if not treated promptly during the acute phase, neurons die at a rate of 2 million per min. Even after revascularization and reperfusion, injury due to the latter can exacerbate the occurrence of ischemic stroke [3]. Reperfusion therapy is one of the primary treatment methods for ischemic stroke. It aims to restore cerebral blood flow to alleviate or prevent brain tissue damage caused by insufficient blood supply [4]. However, certain challenges remain. On one hand, reperfusion therapy itself may trigger ischemia-reperfusion injury, exacerbating oxidative stress and inflammatory responses [5], leading to further damage to brain tissue. On the other hand, reperfusion therapy must be administered within a specific time window after stroke onset to avoid irreversible brain damage [6]. This type of damage is referred to as cerebral ischemia-reperfusion injury (CIRI).

Traditional Chinese Medicine (TCM) contains various active ingredients, which often exhibit complex mechanisms that can effectively treat multi-factorial diseases [7]. However, effective pharmacological treatments for the acute phase of CIRI remain limited, and the blood-brain barrier (BBB) poses a significant challenge by restricting the entry of therapeutic agents into the central nervous system [8,9]. Non-pharmacological approaches, such as electroacupuncture [10], hyperbaric oxygen therapy [11], and transcranial electrical stimulation [12], play important roles in post-stroke rehabilitation but are not suitable for emergency intervention. Intranasal drug delivery offers a promising alternative by bypassing the BBB, providing a fast, convenient, and effective route for treating brain disorders and enhancing patient compliance [13]. Nasal sprays like Naoxing [14] and Tongnao [15] have been shown to improve cerebral circulation and protect neurological functions, demonstrating significant efficacy in treating ischemic brain injury. In recent years, novel nasal formulations, such as nanoliposomes, nanoparticles, microemulsions, and polymeric micelles, have gained attention for their targeting and sustained-release properties [16-18].

Nanoliposomes are artificial vesicles composed of lipid bilayers with diameters ranging from 25 nm to 1000 nm. Due to their structural similarity to cell membranes, liposomes can protect drugs

***Corresponding author:**
E-mail address: chenxiaolan76@126.com (X. Chen)

Received: 09 October, 2024 **Accepted:** 06 March, 2025 **Epub Ahead of Print:** 10 May 2025 **Published:** 21 May 2025
DOI: 10.25259/AJC_76_2024

from enzymatic degradation before reaching the target site while also enhancing drug stability and reducing toxicity. To improve the performance of liposomes (e.g., stability, targeting ability, and long circulation), functional materials are often incorporated. Methoxy poly(ethylene glycol)-poly(lactic acid) (mPEG-PLA) is an amphiphilic polymer material consisting of a hydrophilic mPEG segment and a hydrophobic PLA segment. It exhibits excellent mucus-penetrating properties, facilitating drug transport through the mucus layer into the bloodstream [19]. Additionally, mPEG-PLA is biodegradable *in vivo* and highly biocompatible. With a critical micelle concentration of only 7.71 mg/L [20], it can resist structural damage to liposomes caused by dilution *in vitro* or the aqueous environment *in vivo*. Currently, mPEG-PLA has been widely applied in drug delivery systems. For instance, encapsulating honokiol within mPEG-PLA nanoparticles enables the hydrophobic honokiol to be administered *via* intravenous injection [21]. Curcumin-loaded mPEG-PLA nanoliposome can effectively inhibit the proliferation of A549 cells, increase the cytotoxicity, induce G2/M phase arrest, and promote cell apoptosis [19]. The first approved nanoliposomes of paclitaxel for the treatment of cancer (breast and lung cancer) developed by Samyang Biopharm, a Korean biopharmacological company, use mPEG-PLA as an adjuvant. In the phase I clinical study, the product was used without pretreatment with antihistamines, and no severe allergic reactions occurred. In a phase II clinical study, the product showed significantly improved efficacy compared with paclitaxel injection and paclitaxel albumin nanoparticles [22]. Studies [23] have found that the extracellular LDH content of tumor cells after triptolide (TP)-mPEG-PLA administration is higher than that of the original drug, suggesting that mPEG-PLA can enhance the destruction of the cell membrane by TP. Acute toxicity experiments have shown that mPEG-PLA can expand the therapeutic window of TP and improve the safety of medication [24]. In summary, mPEG-PLA has the potential to be an ideal targeted drug delivery system due to its greatly improved hydropathy and good biodegradability.

Gleditsiae Fructus Abnormalis (GFA), the dried fruit of *Gleditsia sinensis* Lam., is documented in the Chinese Pharmacopoeia for its efficacy in resolving phlegm, relieving swelling, and dispersing stagnation when administered nasally [25]. The main active components include paeonol, eugenol, methyl eugenol, linalool, and anethole, which exhibit anticancer, anti-inflammatory, analgesic, neuroprotective, antioxidant, anti-myocardial ischemia, and antibacterial properties [26-28]. Our previous studies employed GC-MS to identify the primary components of five active components of VOGFA (FVOGFA) [29]. Using network pharmacology and molecular docking, we identified five active components—paeonol, eugenol, methyl eugenol, linalool, and anethole—that target key proteins such as VEGF, TNF-α, Proto-oncogene tyrosine-protein kinase Src (SRC), hosphatidylinositol-4,5-bisphosphate 3-kinase catalytic subunit alpha (PIK3CA), and MAPK8 (mitogen-activated protein kinase 8) related to CIRI. To improve drug delivery, we developed mPEG-PLA nanoliposomes for nasal administration, enhancing BBB permeability and brain targeting. *In vitro* and *in vivo* studies showed these components reduce CIRI by inhibiting inflammation and apoptosis while promoting VEGF expression and angiogenesis. This approach offers a promising solution for emergency ischemic stroke treatment.

2. Materials and Methods

2.1. Materials

Paeonol (GZDD-0046), Eugenol (GZDD-0401), Methyl Eugenol (C102127), Linalool (GZDD-0244), and Anethole (C100243) were procured from Guizhou Dida Technology Co., Ltd., with a purity of over 98%. Nimodipine was obtained from Yabao Pharmaceutical Group Co., Ltd. Soy lecithin PC > 90% (S30869), cholesterol (S11040), and Sephadex G-50 (J18GS151845) were purchased from Shanghai Yuanye Bio-Technology Co., Ltd. Phosphate-buffered saline (PBS, P1003) was sourced from Beijing Solarbio Science & Technology Co., Ltd. mPEG-PLA (molecular weight 2000, 80010401) was acquired from Guangzhou Carbon Water Technology Co., Ltd. Tween 80 (30189828) was obtained from Sinopharm Chemical Reagent Co., Ltd. Dialysis bags MD7034-5 m (molecular weight cutoff 7000, M17J11Y108484) were sourced from Yuanye Bio-Technology Co., Ltd. Methanol (UN1230) was purchased from Sinopharm Chemical Reagent Co., Ltd., and n-Octanol (1607101) was obtained from Shanghai Testsiwei Chemical Co., Ltd. Hematoxylin and eosin staining solutions were sourced from Wuhan Servicebio Technology Co., Ltd. (CR2102133, CR2101094). 2,3,5-Triphenyltetrazolium chloride (TTC, Sigma, 1001011963); rat IL-1β, IL-6, TNF-α ELISA Kits (ZC-36391, ZC-36404, ZC-37624) were purchased from Shanghai Zci Bio-Technology Co., Ltd. VEGF rabbit monoclonal antibody (A12303) was obtained from Abclonal.

2.2. Preparation of FVOGFA-mLP

FVOGFA-mLP were prepared using the ethanol injection method [30]. Soy lecithin, cholesterol, FVOGFA (14 mg, drug-to-soy lecithin ratio 1:13.94, soy lecithin-to-cholesterol ratio 10.77:1), and 15 mg of mPEG-PLA were dissolved in 4 mL ethanol as the oil phase. This was injected into 10 mL PBS (pH 6.40) under magnetic stirring at 900 r/min for 30 mins. After ethanol removal with nitrogen gas, the mixture was filtered through a 0.22 μm membrane, yielding a milky white liposome solution stored at 4°C.

2.3. Encapsulation efficiency and drug loading of FVOGFA-mLP

The encapsulation efficiency (EE) was measured using the Sephadex G-50 gel column method [31]. After adding 0.5 mL of FVOGFA-mLP solution to a pre-treated microcolumn, it was left to stand for 30 mins. PBS (1 mL) was then added, followed by centrifugation at 1000 r/min for 3 mins. The eluate was diluted to 5 mL with methanol, and the peak area was analyzed by HPLC (Welchrom C18 column, methanol-water mobile phase 68:32, flow rate 1 mL/min, detection wavelength 200 nm, injection volume 10 μL, column temperature 30°C). Encapsulation efficiency (EE%) and drug loading (DL) were calculated as follows (Eq. 1):

$$EE\% = \left(\frac{W_{encapsulated}}{W_{total}} \right) \times 100\% \quad (1)$$

$$DL\% = \left(\frac{W_{encapsulated}}{W_{total} + W_{lipid}} \right) \times 100\% \quad (2)$$

$W_{encapsulated}$ is the amount of FVOGFA encapsulated in the mPEG-PLA nanoliposomes (in the eluate), and W_{total} is the total amount of FVOGFA added to the mPEG-PLA nanoliposomes. W_{lipid} is the amount of lipid excipients added to the mPEG-PLA nanoliposomes (Eq. 2).

2.4. Optimization of FVOGFA-mLP preparation by Box-Behnken design

Based on single-factor experiments, three significant factors and their levels were identified, as shown in Table 1 below. The Box-Behnken response surface methodology was used to optimize the formulation by evaluating the effects of the drug-to-soy lecithin ratio (A), soy lecithin-to-cholesterol ratio (B), and mPEG-PLA dosage (C) on the encapsulation efficiency (Y) of the nanoliposomes. Design Expert software was employed to optimize the formulation of FVOGFA-mLP.

2.5. Characterization of FVOGFA-mLP

2.5.1. Analysis of morphology by using transmission electron microscopy (TEM)

The morphology of FVOGFA-mLP was observed using transmission electron microscopy (JEM-1400FLASH transmission electron

Table 1. Factors and responses in Box-Behenken design.

Factors	Levels		
	-1	0	1
A (mg/mg)	1:8	1:12	1:16
B (mg/mg)	8:1	10:1	12:1
C (mg)	7.5	15	30

microscope, Shimadzu, Japan). Samples were stained with 1% phosphotungstic acid (pH 7.0) for 30 seconds, dried, and photographed under the TEM.

2.5.2. Analysis of particle size, polydispersity index, and zeta potentially

The Beckman particle size analyzer (Delsa Maxpro, America) was used to analyze the particle size, polydispersity index, and zeta potential of FVOGFA-mLP nanoliposomes. The prepared samples were diluted 20 times with PBS before the determination. The measurements were performed at a temperature of 25°C. The average values were determined by averaging the results of three measurements for each sample, with 30 runs per measurement.

2.5.3. Analysis of fourier transform infrared spectroscopy (FTIR)

The FTIR spectra of the FVOGFA-mLP freeze-dried products, blank mPEG-PLA nanoliposomes freeze-dried products, and the individual drugs were obtained using an FTIR spectrophotometer (Nicolet iS50, America). The samples were crushed to a fine powder, mulled with anhydrous potassium bromide, pressed to form a thin pellet, and the spectra were obtained in the wavenumber region between 4000 and 400 cm^{-1}.

2.5.4. Analysis of differential scanning calorimetry (DSC)

Thermal analyses of FVOGFA-mLP freeze-dried products, physical mixture of drug, and mPEG-PLA nanoliposomes freeze-dried products, along with the drug mixtures were performed using a differential scanning calorimeter (NETZSCH DSC 3500, German). The samples to be measured were placed sequentially in the corresponding aluminum pans, their weights were recorded, and then nitrogen gas was applied at a flow rate of 60 mL/min. They were heated from 0°C to 200°C at a heating rate of 5°C/min, calibrating/measuring within a range of 0-5000 μV for DSC scanning analysis.

2.6. In vitro *release study of FVOGFA-mLP*

The *in vitro* release of FVOGFA-mLP was assessed using a dialysis bag diffusion method [32]. FVOGFA-mLP (1mL) was placed in a dialysis bag (7000 Da cutoff) and immersed in 40 mL of PBS with 1% Tween 80 (pH 5.5) at 37°C with constant shaking. Samples were taken at specific intervals (10 mins, 20 mins, and 0.5, 2, 4, 6, 8, 10, 12, 20, 28, and 36 hrs), filtered, and replaced with fresh media. The active components were quantified by HPLC, and the cumulative release rates (Q) at different time points were calculated and plotted (Eq. 3).

$$Q = \left(\frac{CnVo + \sum_{i=1}^{n-1} CiVi}{M} \right) \times 100\% \quad (3)$$

V_0 is the total volume of the release medium (mL), V_i is the sampled volume (mL), C_i and C_n are the five active components concentrations (mg/mL) at sampling times i and n, respectively, and M represents the total mass of each component in the sample.

2.7. Stability study of FVOGFA-mLP

Three batches of FVOGFA-mLP samples were stored at 4°C and 25°C in the dark. Samples were taken at 0, 7, 15, 30, 60, and 90 days to measure particle size, polydispersity (PDI), zeta potential, and encapsulation efficiency, evaluating the stability of the FVOGFA-mLP.

2.8. Cell experiments

2.8.1. PC12 cell culture

PC12 cells were routinely cultured in dulbecco's modified eagle medium (DMEM) complete medium, consisting of DMEM supplemented with 10% fetal bovine serum and 1% penicillin-streptomycin, under conditions of 37°C and 5% CO_2.

2.8.2. Establishment of the OGD/R model

PC12 cells were cultured in DMEM complete medium (10% fetal bovine serum, 1% penicillin-streptomycin) at 37°C and 5% CO_2. Logarithmically growing cells were seeded, washed with PBS, and subjected to OGD in earle's balanced salt solution (EBSS) buffer within a tri-gas incubator (94% N_2, 5% CO_2, 1% O_2) for 2 h. Afterward, DMEM complete medium was reintroduced, and the cells underwent 24 hrs of reoxygenation to establish the OGD/R model. The control group followed the same protocol without OGD treatment.

2.8.3. Grouping and treatment

The experiment consisted of six groups: Control, model, nimodipine (2 μg/mL), FVOGFA-L (5 μg/mL), FVOGFA-M (10 μg/mL), FVOGFA-H (20 μg/mL). The Control group was normally cultured without treatment, while the other groups underwent 2 h of OGD followed by 24 hrs of reoxygenation and glucose reintroduction. All drug treatment groups were pre-incubated with the respective drugs for 2 h before modeling.

2.8.4. Cell viability assay

PC12 cells were seeded in 96-well plates at approximately 8,000 cells per well. Each drug treatment group was pre-incubated for 2 h before undergoing OGD/R treatment. Subsequently, 10 μL of CCK8 solution was added to each well, and the plates were incubated at 37°C for 2 h. Absorbance was measured at 450 nm using a microplate reader (Shanghai Mapada Instruments Co., Ltd., UV-6100 double beam spectrophotometer, China). Relative cell viability was calculated with the formula (Eq. 4):

$$\text{Relative cell viability} = \left(\frac{\text{Experimental Group} - \text{Blank Group}}{\text{Control Group} - \text{Blank Group}} \right) \times 100\% \quad (4)$$

2.8.5. Measurement of IL-1β, IL-6, and TNF-α in cell supernatants

After 24 hrs of reoxygenation and glucose reintroduction, the supernatants of each group were collected and centrifuged at 4°C for 10 mins. The levels of IL-1β, IL-6, and TNF-α were measured using enzyme-linked immunosorbent assay (ELISA) kits according to the manufacturer's instructions, with absorbance measured at 450 nm. Concentrations were calculated based on a standard curve.

2.8.6. Cell migration assay

Cell migration was assessed using a scratch assay. PC12 cells were seeded in 6-well plates at a density of 1×10^5 cells/mL. Following OGD/R treatment, a 200 μL pipette tip was used to create a scratch in each well. Images of the scratch area were taken at 0, 12, and 24 hrs. The images were analyzed with ImageJ software to calculate the cell migration rate using the formula (Eq. 5):

$$\text{Cell Migration Rate} = \left(\frac{\text{Initial Scratch Area} - \text{Scratch Area at a Time t}}{\text{Initial Scratch Area}} \right) \times 100\% \quad (5)$$

2.8.7. Flow cytometry analysis

After OGD/R treatment, the medium was discarded, and the cells were digested with trypsin without ethylenediaminetetraacetic acid (EDTA). The cells were collected, centrifuged at 2,000 r/min for 5 mins, washed twice with sterile PBS, and centrifuged again. The supernatant was discarded, and the cells were resuspended in 250-500 μL of binding buffer. The suspension was incubated in the dark with 5 μL Annexin validity-fluorescein isothiocyanate (V-FITC) and 5 μL propidium iodide (PI) for 5-10 mins at room temperature, followed by flow cytometry analysis (Accuri C6 Plus Flow Cytometer, BD, America) for cell cycle and apoptosis.

2.8.8. Detection of apoptosis by Annexin V-FITC/PI staining

PC12 cells underwent 24 hrs of reoxygenation and glucose reintroduction. Afterward, the medium was discarded, and the cells were washed twice with pre-cooled PBS. Cells were incubated with Annexin V-FITC reagent (10 μL per well) for 15 mins, followed by the addition of 5 μL propidium iodide (PI) solution for 5 mins, both in the dark. After washing twice with PBS, apoptosis was observed under a fluorescence microscope, with live cells showing green fluorescence and dead cells red fluorescence.

2.8.9. Immunofluorescence detection of VEGF expression

PC12 cells from each treatment group were pre-incubated with respective drugs for 2 hrs before undergoing 24-hour OGD/R treatment. After treatment, cells were fixed with 4% paraformaldehyde for 30 mins, washed, permeabilized, and blocked with 1% bovine serum albumin (BSA) for 1 hr. They were then incubated overnight with Beclin-1 antibody (1:100) at 4°C, followed by incubation with a fluorescent secondary antibody (1:300) for 50 mins. After 4′,6-diamidino-2-phenylindole (DAPI) staining and mounting, VEGF expression was quantified using ISCapture software by measuring the average and integrated optical densities from the images.

2.8.10. In vitro *transmembrane penetration assay*

To assess the transmembrane penetration of FVOGFA-mPL, PC12 cells were seeded at 2.5×10^5 cells/mL in 0.5 mL on a Transwell plate. Diluted FVOGFA and FVOGFA-mPL solutions (1:10) were prepared in DMEM, with 500 μL added to the upper chamber and 1500 μL to the lower chamber. At specific time points (0.25, 0.5, 1, 2, 4, and 8 hrs), 450 μL of the upper chamber medium was collected, mixed with methanol, and ultrasonically mixed. The transmembrane transport of FVOGFA-mPL was quantified *via* HPLC.

2.9. Animal experiments

2.9.1. Animals

A total of 96 male Sprague-Dawley rats (250-280g, SPF grade) were obtained from Henan Sikebeisi Biotechnology Co., Ltd. (Certificate No. SCXK (Yu) 2020-0005). Quality control was verified by the Institute of Laboratory Animal Science, Chinese Academy of Medical Sciences. Rats were housed under standardized conditions: temperature maintained at 25°C, relative humidity at 50-60%, and a 12-hour light/dark cycle. The animals had free access to food and water and were allowed a 7-day acclimatization period. All experimental procedures were approved by the Animal Ethics Committee of Guizhou University of Traditional Chinese Medicine (Approval No. 20210046).

2.9.2. Grouping and administration

Rats were randomly divided into eight groups (n=12 per group): control, sham-operated, model, blank-mLP groups, nimodipine (5.83 mg/kg), FVOGFA-mLP-L (0.028 mg/kg), FVOGFA-mLP-M (0.056 mg/kg), FVOGFA-mLP-H (0.108 mg/kg).

2.9.3. Induction of cerebral ischemia-reperfusion injury

CIRI was induced using the modified middle cerebral artery occlusion (MCAO) method. After anesthetizing the rats with 20% urethane, a midline cervical incision exposed the left carotid arteries and vagus nerve. The proximal common carotid artery (CCA) was ligated, and the distal CCA and external carotid artery (ECA) were clamped. A monofilament nylon suture was inserted into the internal carotid artery (ICA) to a depth of 18.0 ± 1.0 mm and secured. After 2 hrs, the suture was partially retracted for reperfusion. In the sham group, vessels were exposed, but no suture was inserted. Rats received optimal post-surgical care.

2.9.4. Neurological function assessment

Neurological deficits were evaluated 24 hrs post-surgery using the Longa scoring system (Table 2).

Table 2. Longa neurological score.

Neurological Behavior	Score
No neurological deficit	0 (Normal)
Incomplete extension of the contralateral forepaw when tail is lifted	1 (Mild)
Circling to the contralateral side when walking	2 (Moderate)
Falling to the contralateral side when standing or walking	3 (Severe)
Unable to walk, unconscious	4 (Very severe)

2.9.5. TTC staining to determine infarct volume

Following neurological assessment, the rats were anesthetized and decapitated. Brain tissues were rapidly removed, frozen at -20°C for 20 mins, and then sectioned coronally at 2 mm intervals. Sections were incubated with 2% TTC solution at 37°C in the dark for 30 mins, ensuring uniform staining by flipping the sections. Infarct volume was analyzed using Image J software (Eq. 6).

$$\text{Infarct volume percentage} = (\text{Infarct area}/\text{Total brain area}) \times 100\% \quad (6)$$

2.9.6. Hematoxylin-eosin staining to assess brain morphology

Brain tissue from the infarcted motor cortex was washed with PBS, fixed with 4% paraformaldehyde, dehydrated with graded ethanol (50%-100%), embedded in paraffin, sectioned, deparaffinized, and rehydrated with graded ethanol. Sections were stained with hematoxylin and eosin, dehydrated again with ethanol, cleared with xylene, mounted with resin, and observed under a light microscope to assess morphological changes.

2.9.7. ELISA for detection of IL-1β, IL-6, and TNF-α

After 24 hrs of reperfusion, rats from each group were decapitated, and the ischemic hemispheres were quickly excised and homogenized in an ice-cold buffer to prepare 10% brain homogenates. The homogenates were centrifuged at 3000 r/min for 10 mins. Brain tissue levels of IL-1β, IL-6, and TNF-α were quantified using ELISA kits according to the manufacturer's instructions.

2.9.8. Immunofluorescence for VEGF, $CD31^+$/$Ki67^+$ expression

Brain tissue from the periinfarct area was sectioned and subjected to antigen retrieval, permeabilized with Triton X-100, and blocked with BSA. Sections were incubated overnight with BrdU and NeuN antibodies, followed by Coralite 594-conjugated secondary antibodies. After washing and mounting, fluorescence images were captured, and VEGF and $CD31^+$/$Ki67^+$ expression were quantified using Image J software.

2.9.9. Western blot for SRC, MAPK8, PIK3CA, and TNF protein expression

Frozen brain tissue from the left infarct area was lysed in radioimmunoprecipitation assay (RIPA) buffer, centrifuged, and protein concentration was measured. After Sodium Dodecyl Sulfate - PolyAcrylamide Gel Electrophoresis (SDS-PAGE) and protein transfer to polyvinylidene difluoride (PVDF) membranes, membranes were blocked, incubated overnight with primary antibodies (SRC, MAPK8, PIK3CA, TNF), and then with horseradish peroxidase (HRP)-conjugated secondary antibodies. Bands were visualized using enhanced chemiluminescence (ECL) and quantified with Alpha Innotech imaging, with intensities normalized to Glyceraldehyde-Aldehyde-3-Phosphate Dehydrogenase (GAPDH).

2.9.10. qRT-PCR for VEGF and HIF-1α mRNA expression

Total RNA was extracted from brain tissue, and cDNA was synthesized using a reverse transcription kit. quantitative real-time polymerase chain reaction (qRT-PCR) was performed to measure VEGF and HIF-1α mRNA levels, with β-actin as an internal control. Each sample was tested in triplicate. Relative gene expression was calculated using the comparative Ct method. Primer sequences have been listed in Table 3.

Table 3. Primer sequence.

Gene	Primer sequence (5'->3')	Product length (bp)
HIF-1a	ACAGGATTCCAGCAGACCC	186
	TGATGCCTTAGCAGTGGTC	
VEGF	CGAGGAAAGGGAAAGGGTC	91
	TTCTCCGCTCTGAACAAGG	
β-actin	AGATTACTGCCCTGGCTCCTAG	144
	CATCGTACTCCTGCTTGCTGAT	

2.9.11. In vivo *imaging*

Institute of cancer research (ICR) mice were anesthetized, and the head was completely shaved. FVOGFA-mLP was labeled with Cy7, an infrared fluorescent probe. Mice were divided into four groups: control, Cy7+FVOGFA, Cy7+FVOGFA-mLP, and MCAO+Cy7+FVOGFA-mLP. The Cy7 concentration was 1 mg/mL, and 10 μL was administered intranasally. Mice were housed individually to avoid cross-contamination of fluorescence. Fluorescence imaging was performed at 10, 30, 60, 120, and 360 mins using excitation and emission wavelengths of 750 nm and 780 nm, respectively.

2.10. Statistical analysis

Data were expressed as mean ± standard deviation ($\bar{x} \pm s$). Statistical analyses were performed using SPSS 25.0 and GraphPad Prism 8.0. The t-test was used for comparison between two groups, while one-way ANOVA was used for comparison among multiple groups. $p < 0.05$ was considered statistically significant, and $p < 0.01$ was considered highly significant. $p > 0.05$ indicated no significant difference.

3. Results and Discussion

3.1. Preparation and optimization of FVOGFA-mLP

This section compares two widely used methods for nanoliposome preparation: the thin-film dispersion method and the ethanol injection method. The results (Table 4) demonstrated that nanoliposomes prepared using the ethanol injection method exhibited a higher encapsulation efficiency. Furthermore, during the preparation process, the thin-film dispersion method resulted in minor flocculent precipitates during hydration, while the ethanol injection method produced a clear and transparent nanoliposome solution. Based on these findings, the ethanol injection method was chosen for subsequent experiments.

Using Design Expert 8.0.6.1 software, the experimental results were analyzed through data fitting and ANOVA to evaluate the response surface parameters (Table 5). This analysis established a polynomial equation correlating the overall encapsulation efficiency (Y) with the ratio of drug to soybean lecithin (A), the ratio of soybean lecithin to cholesterol (B), and mPEG-PLA dosage (C):

$$Y=67.07+6.83A+3.50B+1.49C+2.25AB+6.86AC+4.50BC-13.81A^2-8.45B^2-2.45C^2$$

The significance test results have been presented in Table 6. Regression analysis identified that the factors significantly influencing encapsulation efficiency were A, AC, A^2, and B^2 ($p < 0.05$), while B ($p = 0.1259$) and C ($p = 0.4842$) were not statistically significant. The factors ranked in order of influence as A > B > C. The model's p-value of 0.0096 indicated strong statistical significance, with a correlation coefficient (R^2) of 0.8977, reflecting high predictive accuracy and a strong correlation between observed and predicted values. The goodness-of-fit test p-value of 0.0526 further confirmed the model's suitability. Overall, the polynomial equation effectively simulates the conditions for nanoliposome preparation and is appropriate for further analysis.

Table 4. Screening results of preparation methods.

Compound	Encapsulation efficiency (%)	
	Thin-film dispersion method	Ethanol injection method
Paeonol	14.71±0.79	41.47±2.67
Eugenol	56.43±2.12	52.55±1.91
Methyl Eugenol	34.38±1.41	54.82±1.38
Linalool	21.25±1.66	45.53±1.13
Anethole	45.51±2.28	46.06±1.29
Overall	28.80	45.15

Table 5. Scheme of Box-Behenken Design with the results of responses on three independent factors.

No.	Independent variables			Dependent variables
	A	B	C	Y
1	1:8	8:1	15	32.91
2	1:16	8:1	15	43.11
3	1:8	12:1	15	42.02
4	1:16	12:1	15	61.22
5	1:8	10:1	7.5	53.38
6	1:16	10:1	7.5	52.27
7	1:8	10:1	30	35.63
8	1:16	10:1	30	61.95
9	1:12	8:1	7.5	55.49
10	1:12	12:1	7.5	46.87
11	1:12	8:1	30	56.47
12	1:12	12:1	30	65.86
13	1:12	10:1	15	61.8
14	1:12	10:1	15	69.89
15	1:12	10:1	15	68.36
16	1:12	10:1	7.5	68.42
17	1:12	10:1	15	66.88

Table 6. Regression model analysis of variance.

Source	Sum of squares	df	Mean square	*F* value	*p*-value Prob > *F*	
Model	1993.69	9	221.52	6.83	0.0096	Significant
A	372.78	1	372.78	11.49	0.0116	
B	97.93	1	97.93	3.02	0.1259	
C	17.70	1	17.70	0.55	0.4842	
AB	20.25	1	20.25	0.62	0.4555	
AC	188.10	1	188.10	5.80	0.0469	
BC	81.09	1	81.09	2.50	0.1580	
A^2	803.02	1	803.02	24.74	0.0016	
B^2	300.29	1	300.29	9.25	0.0188	
C^2	25.33	1	25.33	0.78	0.4063	
Residual	227.17	7	32.45			
Lack of fit	187.93	3	62.64	6.38	0.0526	Not significant
Pure error	39.25	4	9.81			
Cor total	2220.86	16				

Significant $p < 0.05$, Not significant > 0.05.

3.2. Response surface and optimization

Response surface plots based on the polynomial regression results (Figure 1) indicated that encapsulation efficiency initially increased but then declined as the ratio of drug to soybean lecithin and the ratio of soybean lecithin to cholesterol increased. When the drug-to-soybean

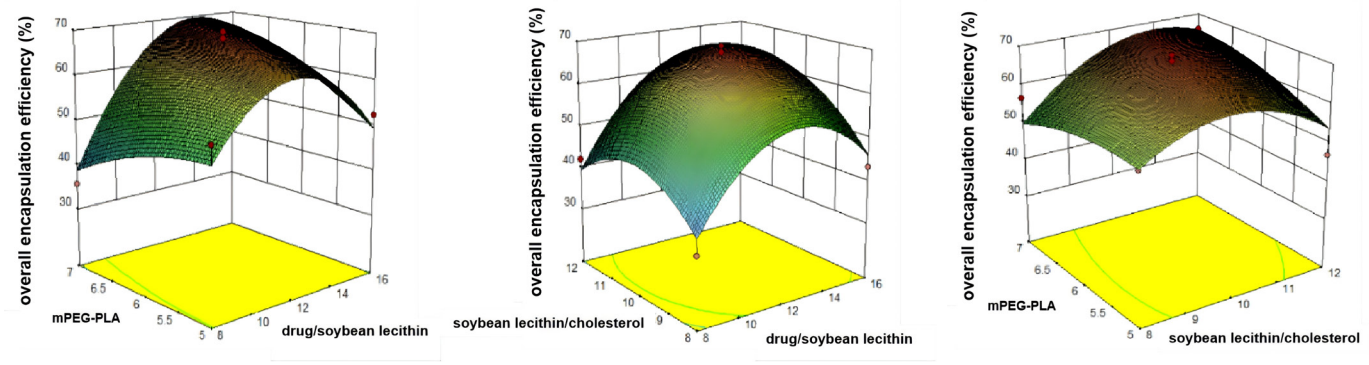

Figure 1. Three-dimensional response surface diagrams. Response surface diagrams of overall encapsulation efficiency.

Table 7. The FVOGFA-mLP validation test.

Compound	Encapsulation efficiency (%), n = 3		
Paeonol	70.5	67.3	71.1
Eugenol	69.1	74.0	70.3
Methyl Eugenol	65.0	68.5	62.8
Linalool	86.2	86.7	79.9
Anethole	63.3	66.0	62.9
Overall	71.39		

lecithin ratio exceeded 1:12, encapsulation efficiency began to decrease, likely due to nanoliposome saturation. Similarly, encapsulation efficiency dropped as the soybean lecithin-to-cholesterol ratio neared 10:1, possibly because excess cholesterol increases membrane asymmetry, permeability, and rigidity. Additionally, a dosage of 15 mg of mPEG-PLA demonstrated optimal encapsulation efficiency.

The optimized conditions, as determined by the response surface method, included a drug-to-soybean lecithin ratio of 1:13.94, a soybean lecithin-to-cholesterol ratio of 10.77:1, and mPEG-PLA dosage of 15 mg, predicting an encapsulation efficiency of 69.89%. To validate these conditions, three batches of nanoliposomes were prepared using the optimized process. As shown in Table 7, the prepared mPEG-PLA nanoliposome solution had a satisfactory appearance, and the formulation's reproducibility achieved an encapsulation efficiency of 71.39%. The deviation between predicted and experimental values was -1.5%, demonstrating the high reliability of the polynomial model.

3.3. Characterization of FVOGFA-mLP

The FVOGFA-mLP appeared as a uniform and stable milky white suspension, with no precipitation and no noticeable or unpleasant odor (Figure 2a). TEM images showed that the FVOGFA-mLP were predominantly spherical or spheroidal in shape, with consistent morphology and well-dispersed particles, exhibiting no signs of aggregation (Figures 2b and 2c). The average particle size of the FVOGFA-mLP was 182.33 ± 0.72 nm, with a polydispersity index (PDI) of 0.24 ± 0.06 and a zeta potential of -15.66 ± 0.92 mV (Figure 2d). These values indicate a uniform particle size distribution and negatively charged surface, which enhanced electrostatic repulsion between the mPEG-PLA nanoliposomes, reducing aggregation and fusion during storage and thus improving stability. Moreover, the PEG chains in mPEG-PLA form a hydrophilic protective layer on the surface of the nanoliposomes, further enhancing their stability and uniformity.

The infrared spectra of individual drugs and liposomal formulations reveal significant insights into their molecular characteristics and interactions (Figure 2e). The spectra of linalool, anethole, paeonol, eugenol, and methyl eugenol exhibited distinct peaks associated with their functional groups, such as C-H stretching (2800 cm^{-1}), C=C stretching (1600 cm^{-1}), and C=O stretching (1700 cm^{-1}). In contrast, the blank mPEG-PLA nanoliposome spectrum primarily reflected lipid-specific vibrations, with broad peaks around 1000-1500 cm^{-1}, typical for lipid bilayers. However, the spectrum of the FVOGFA-mLP showed notable shifts and intensified peaks, particularly in the 1000-1500 cm^{-1} region, indicating structural alterations in the lipid bilayer due to drug encapsulation. These changes suggest that drug-lipid interactions significantly modify the liposomal structure, potentially affecting membrane dynamics and drug release characteristics.

Comparative differential scanning calorimetry (DSC) analysis of three formulations—drug mixtures (DM), drug-mPEG-PLA-LP mixtures (DMPM), and FVOGFA-mLP—reveals distinct thermal behavior governed by carrier interactions and nanostructuring (Figure 2f). Drug mixtures exhibited a broad endothermic peak (onset 43.4°C, ΔH=13.27 J/g), indicative of disordered drug crystallization. Drug-mPEG-PLA-LP mixtures showed delayed phase transition onset (68.2°C), widened thermal window (73.6°C), and reduced ΔH (10.1 J/g), suggesting suppressed crystallinity due to hydrophobic/H-bond interactions between drug and carrier. FVOGFA-mLP displayed a sharp peak (117.5°C, ΔH > DCM) with a narrow width (13.8°C), implying synchronous phase transition driven by lipid bilayer confinement. This hierarchy—drug mixtures (amorphous) → drug mPEG-PLA-LP mixtures (DMPM) (interaction-limited crystallization) → FVOGFA-mLP (nanostructured co-transition)—highlights that carrier modulation shifts drug release from passive diffusion (DM) to interaction-mediated retardation (DMPM) and lipid-membrane-coupled burst release (FVOGFA-mLP), offering a thermal roadmap for tunable drug delivery.

3.4. In vitro *release studies*

The *in vitro* release profile of FVOGFA-mLP was compared to that of an FVOGFA-PBS solution, as shown in Figure 3. Within the first 10 mins, approximately 20% of paeonol, eugenol, methyl eugenol, linalool, and anethole were released from FVOGFA-mLP. After 30 mins, a noticeable divergence in release profiles emerged, with the active compounds encapsulated in mPEG-PLA nanoliposomes releasing more slowly than those in the PBS solution. This suggests that the mPEG-PLA nanoliposomes began releasing the five compounds after the 30-min mark. In PBS solution, all compounds were nearly fully released (close to 100%) within 12 hrs, whereas in the nanoliposomes, the compounds exhibited an initial rapid release phase followed by a slower, sustained release. The cumulative release of the first four compounds exceeded 90% within 36 hrs, while anethole reached 79% release over 48 hrs. These findings demonstrate that FVOGFA-mLP effectively prolongs drug release, offering significant sustained-release properties.

To further analyze the release behavior of FVOGFA-mLP, the release curves were fitted to five common release models (Tables 8-12), with the best fit determined by the coefficient of determination (R^2). The results indicated that the Higuchi, Weibull, and Ritger-Peppas models had R^2 values greater than 0.9, with the Weibull model showing the highest fit ($R^2 > 0.97$). This suggests that the mPEG-PLA nanoliposomes exhibit excellent sustained-release performance.

3.5. Stability studies

Over 90 days, FVOGFA-mLP stored at 4°C in the dark exhibited good stability (Figure 4). The particle size remained stable, ranging

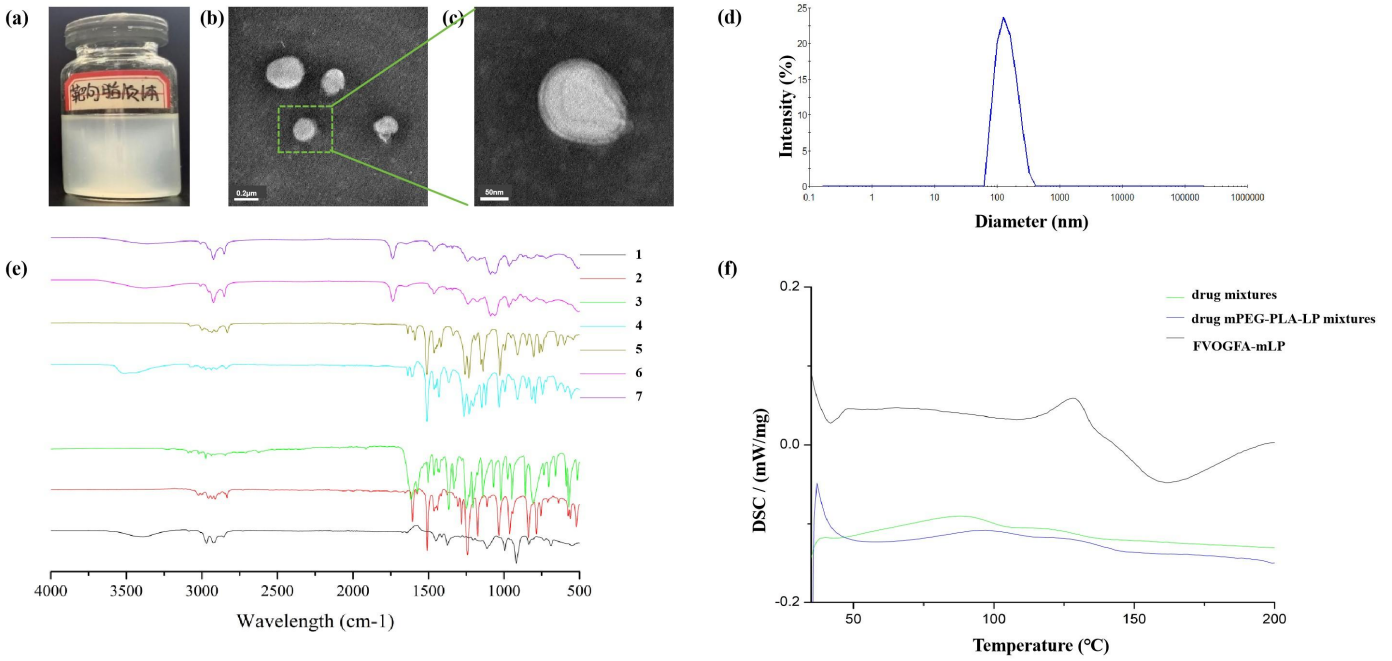

Figure 2. Characterization of FVOGFA-mLP. (a) The appearance of FVOGFA-mLP; (b) the TEM photograph of FVOGFA-mLP (Scale bar = 0.2 μm); (c) the TEM photograph of FVOGFA-mLP (scale bar = 50 nm); (d) the size distribution of FVOGFA-mLP. (e) FTIR spectrum of (1) Linalool, (2) Anethole, (3) Paeonol, (4) Eugenol, (5) Methy Eugenol, (6) blank mPEG-PLA nanoliposome and (7) FVOGFA-mLP nanoliposome; (f) the DSC chromatogram.

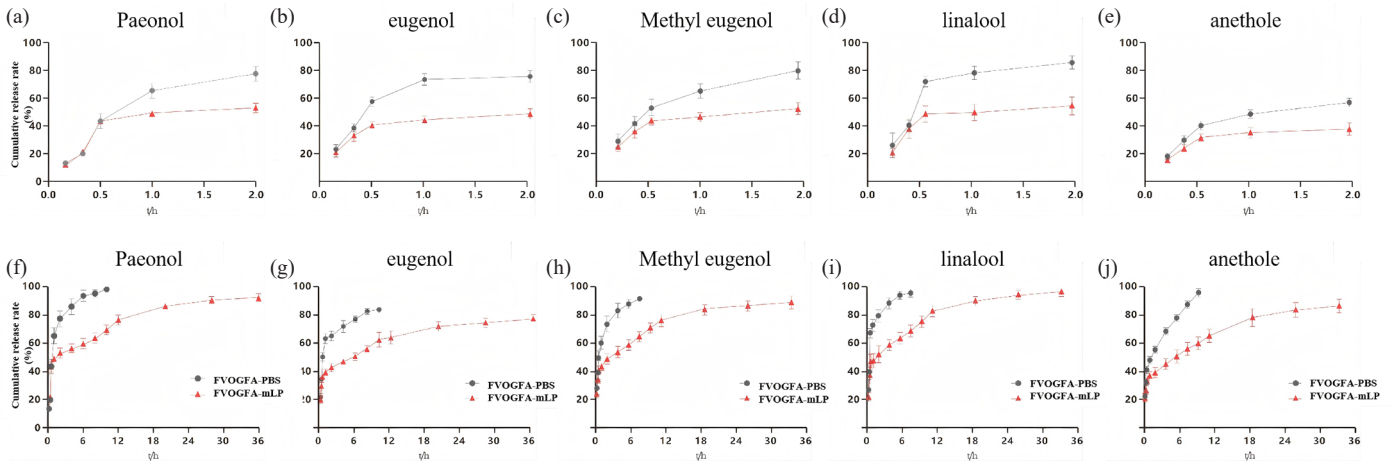

Figure 3. *In vitro* release profiles of FVOGFA and FVOGFA-mLP. The cumulative release rates of each component (a-e) within 2 hrs and (f-j) within 36 hrs.

Table 8. *In vitro* release simulation of Paeonol in FVOGFA-mLP nanoliposomes.

Compound	Model	Fitting equation	R^2
Paeonol	Zero-order	Q(t)=1.82 t+43.97	0.66
	First-order	Q(t)=76.80(1-e-1.08 t)	0.77
	Higuchi	Q(t)=12.73 t0.5+28.42	0.84
	Weibull	Q(t)=488.66(1-e(-(2.55(t-0.16))^0.22)	0.97
	Riger-peppas	Q(t)=42.17(t^0.24)	0.91

Table 9. *In vitro* release simulation of Eugenol in FVOGFA-mLP nanoliposomes.

Compound	Model	Fitting equation	R^2
Eugenol	Zero-order	Q(t)=1.62 t+43.64	0.76
	First-order	Q(t)=71.52(1-e-1.30 t)	0.65
	Higuchi	Q(t)=11.19 t0.5+30.59	0.92
	Weibull	Q(t)=985.83(1-e(-(2.79(t-0.13))^0.20)	0.98
	Riger-peppas	Q(t)=42.12(t^0.01)	0.96

Table 10. *In vitro* release simulation of Methyl Eugenol in FVOGFA-mLP nanoliposomes.

Compound	Model	Fitting equation	R^2
Methyl Eugenol	Zero-order	Q(t)=1.74 t+45.61	0.76
	First-order	Q(t)=75.96(1-e-1.17 t)	0.64
	Higuchi	Q(t)=12.01 t0.5+30.60	0.93
	Weibull	Q(t)=1076.13(1-e(-(4.76(t-0.01))^0.22)	0.98
	Riger-peppas	Q(t)=43.92(t^0.22)	0.96

Table 11. *In vitro* release simulation of Linalool in FVOGFA-mLP nanoliposomes.

Compound	Model	Fitting equation	R^2
Linalool	Zero-order	Q(t)=1.84 t+46.21	0.75
	First-order	Q(t)=77.93(1-e-1.18 t)	0.64
	Higuchi	Q(t)=12.61 t0.5+31.56	0.92
	Weibull	Q(t)=1175.11(1-e(-(2.39(t-0.14))^0.21)	0.97
	Riger-peppas	Q(t)=44.51(t^0.23)	0.95

Table 12. *In vitro* release simulation of Anethole in FVOGFA-mLP nanoliposomes.

Compound	Model	Fitting equation	R^2
Anethole	Zero-order	Q(t)=1.88 t+30.62	0.85
	First-order	Q(t)=77.75(1-e-0.19 t)	0.72
	Higuchi	Q(t)=12.56 t0.5+16.56	0.93
	Weibull	Q(t)=1657.83(1-e(-(3.36(t+0.07))^0.32)	0.98
	Riger-peppas	Q(t)=29.02(t^0.31)	0.96

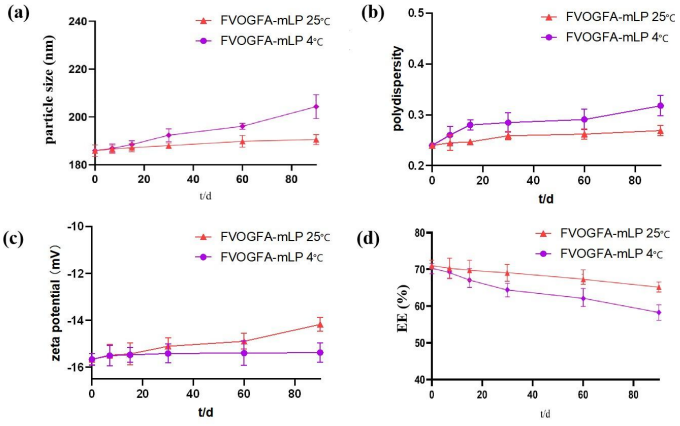

Figure 4. The stability test of FVOGFA-mLP in 90 days. (a) The tendency of the particle size, (b) polydispersity, (c) zeta potential, and (d) the overall encapsulation efficiency of the FVOGFA-mLP.

between 186 and 190 nm, polydispersity was maintained at around 0.2, and the zeta potential was maintained at about -15 mV. The encapsulation efficiency decreased by less than 5%, indicating minimal variation. However, when stored at 25°C in the dark, the particle size, polydispersity, and zeta potential increased markedly, underscoring the considerable effect of temperature on nanoliposome stability. Moreover, the encapsulation efficiency also declined significantly. Thus, storing FVOGFA-mLP at 4°C in the dark is recommended as the optimal storage condition.

3.6. Enhanced effects of FVOGFA on PC12 cell survival and migration following OGD/R

This study explored the protective effects of VOGFA on PC12 cell survival and migration after OGD/R. Initial results indicated that varying the exposure time and dosage of VOGFA did not significantly affect PC12 cell survival rates ($p > 0.05$) (Figure 5a). Consequently, VOGFA was diluted into 5x, 10x, and 20x concentrations, representing high, medium, and low dosage groups for further experiments. After 24 hrs of OGD/R, both the nimodipine and VOGFA-treated groups exhibited a significant increase in PC12 cell survival compared to the model group, with the nimodipine group showing the most notable improvement ($p < 0.01$). In the VOGFA groups, the low-dosage group (VOGFA-L) significantly enhanced cell survival ($p < 0.05$), while the medium (VOGFA-M) and high-dosage (VOGFA-H) groups showed even more pronounced improvements ($p < 0.01$) (Figure 5b).

In terms of cell cycle regulation, FVOGFA also demonstrated a positive impact on PC12 cell proliferation following OGD/R treatment (Figure 5c, Table 13). Flow cytometry revealed that the model group had a significantly higher proportion of cells in the G1 phase ($p < 0.01$) and a lower proportion in the S phase ($p < 0.05$) compared to the control group. The nimodipine group significantly reduced the

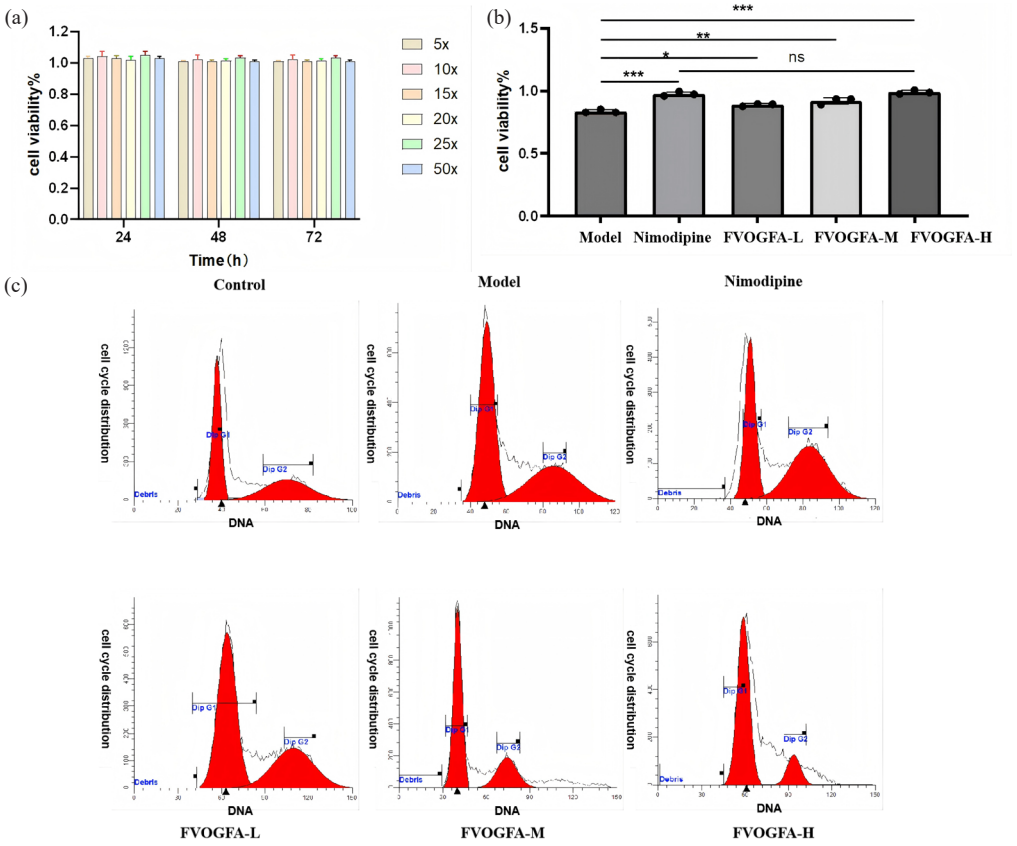

Figure 5. The effects of different exposure time and dosage of VOGFA on PC12 cell survival (a) and (b) following OGD/R , (c) the influences of VOGFA on PC12 cell cycle distribution after OGD/R. Compared with the model group: $^{*}p < 0.05$, $^{**}p < 0.01$, $^{***}p < 0.001$.

Table 13. Comparison of the percentage of cells in G1, S and G2 phases in each group ($\bar{x}\pm s$).

Group	G1	S	G2
Control	36.58±2.4	30.57±3.35	31.68±4.31
Model	65.93±2.86**	14.86±0.98*	17.03±1.01
Nimodipine	42.60±1.10##	31.33±1.43###	23.35±1.98
EOGFA-L	54.82±2.24#	18.84±3.16	24.50±1.82#
EOGFA-M	52.08±0.21#	25.96±0.68###	18.95±1.77
EOGFA-H	47.08±1.23#	25.33±2.18#	25.51±3.36

Data are presented as mean ± SD. Comparisons were made as follows:
Compared with the control group: *p < 0.05, **p < 0.01.
Compared with the model group: #p < 0.05, ##p < 0.01, ###p < 0.001.

percentage of G1 phase cells ($p < 0.01$) and increased the percentage of cells in the S phase ($p < 0.01$) relative to the model group. Similarly, all VOGFA-treated groups showed a significant reduction in G1 phase cells ($p < 0.05$). Furthermore, the medium and high-dosage groups exhibited significant increases in S phase cells ($p < 0.01$ and $p < 0.05$, respectively). These results suggest that FVOGFA facilitates the transition of cells into the S and G2 phases, thereby enhancing DNA synthesis and promoting PC12 cell proliferation in a dose-dependent manner.

The cell scratch assay results (Figures 6a-c) demonstrated that FVOGFA significantly enhances the migration ability of PC12 cells. In the model group, the scratch area increased notably at both 12 and 24 hrs compared with the control group ($p < 0.01$). In contrast, the nimodipine group showed a significant reduction in the scratch area over time, with lowering observed at both 12 and 24 hrs compared with the model group ($p < 0.05$, $p < 0.01$).

For the FVOGFA-treated groups, the low and medium dosages did not show a significant difference in scratch area at 12 hrs compared to the model group. However, the high-dosage group (FVOGFA-H) exhibited significantly enhanced cell migration at 12 hrs compared to the low and medium dosage groups ($p < 0.01$). By 24 hrs, all FVOGFA dosage groups demonstrated a significantly higher cell migration rate compared to the model group ($p < 0.01$). These results indicate that FVOGFA significantly enhances cell migration, with the effects becoming more pronounced over time and at higher dosages.

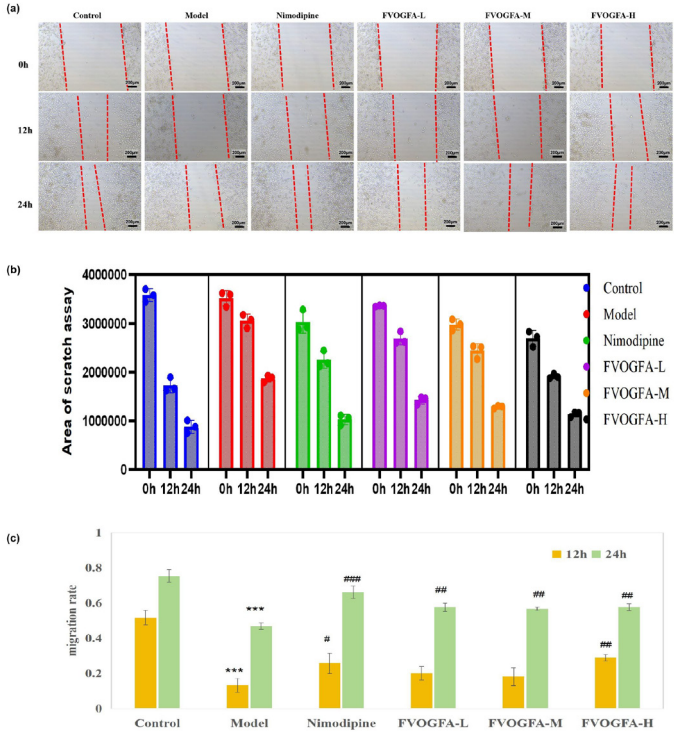

Figure 6. (a) Effects of FVOGFA on the migration of PC12 cells after OGD/R injury (scale bar = 200 μm), (b) the results of area of PC12 cell scratch assay, (c) the PC12 cell migration rates in different groups. Compared with the control group: *p < 0.05, **p < 0.01, ***p < 0.001. Compared with the model group: #p < 0.05, ##p < 0.01, ###p < 0.001.

3.7. FVOGFA significantly reduces apoptosis and enhances cell survival in PC12 cells following OGD/R injury

Apoptosis plays a critical role in CIRI. In this study, Annexin V-FITC/PI double staining was employed to evaluate the effects of FVOGFA on apoptosis in PC12 cells subjected to OGD/R treatment. The results revealed that cells in the control group exhibited healthy growth with minimal apoptosis, whereas the OGD/R model group showed a significantly higher number of apoptotic cells. Pretreatment with nimodipine and various doses of FVOGFA significantly reduced apoptosis in PC12 cells compared to the model group. Notably, there was no significant difference between the high-dosage FVOGFA (FVOGFA-H) group and the nimodipine group, indicating that FVOGFA effectively mitigates OGD/R-induced cell damage by inhibiting apoptosis (Figure 7a).

Flow cytometry further confirmed these findings, showing that nimodipine and all doses of FVOGFA reduced apoptosis to varying degrees (Figures 7b and 7c). In the model group, early and late apoptosis rates were significantly elevated compared to the control group ($p < 0.01$), while necrosis rates did not show a statistically significant difference ($p > 0.05$). Nimodipine treatment significantly reduced both early and late apoptosis ($p < 0.01$) without affecting necrosis rates. FVOGFA demonstrated a more pronounced effect on reducing late apoptosis than early apoptosis. Low, medium, and high doses of FVOGFA significantly reduced late apoptosis ($p < 0.01$) compared to the model group, while the medium and high doses also significantly reduced early apoptosis ($p < 0.05$, $p < 0.01$, respectively).

These findings suggest that FVOGFA offers protective effects by reducing both early and late apoptosis, thereby enhancing the survival of PC12 cells following OGD/R injury. The dose-dependent reduction in apoptosis highlights the potential of FVOGFA as an effective therapeutic agent for ischemia/reperfusion-related injuries.

3.8. FVOGFA significantly alleviates inflammatory damage to PC12 cells induced by OGD/R by inhibiting inflammatory cytokines and increasing VEGF expression

FVOGFA effectively reduces the production of inflammatory cytokines in PC12 cells following OGD/R injury (Figures 8a-c). The results showed that the control group had low levels of IL-1β, IL-6, and TNF-α in the cell supernatant. In contrast, the model group exhibited significantly elevated levels of these cytokines compared to the control group ($p < 0.01$). However, treatment with nimodipine, as well as FVOGFA at high, medium, and low doses, significantly reduced the levels of IL-1β, IL-6, and TNF-α in both the cells and the supernatant when compared to the model group ($p < 0.01$). These findings suggest that FVOGFA alleviates OGD/R-induced inflammatory damage in PC12 cells by inhibiting the production of key inflammatory cytokines. The improvements observed in the medium- and high-dose FVOGFA groups were comparable to those in the nimodipine group.

In addition to reducing inflammation, FVOGFA significantly enhances VEGF expression in PC12 cells after OGD/R injury (Figures 8d-f). VEGF expression was present across the control, model, and treatment groups. Following OGD/R, both the integrated optical density (IOD) and average optical density (AOD) were significantly reduced in the model group compared to the control group ($p < 0.01$), indicating a marked decrease in VEGF expression after injury. However, the nimodipine group and all FVOGFA dose groups showed a significant increase in both IOD and AOD compared to the model group ($p < 0.01$), with VEGF expression increasing in a dose-dependent manner in the FVOGFA groups. Notably, the high-dose FVOGFA group exhibited superior VEGF expression compared to the nimodipine group. These results demonstrate that FVOGFA not only suppresses the production of inflammatory cytokines but also enhances VEGF expression, providing a dual protective effect in alleviating OGD/R-induced damage in PC12 cells.

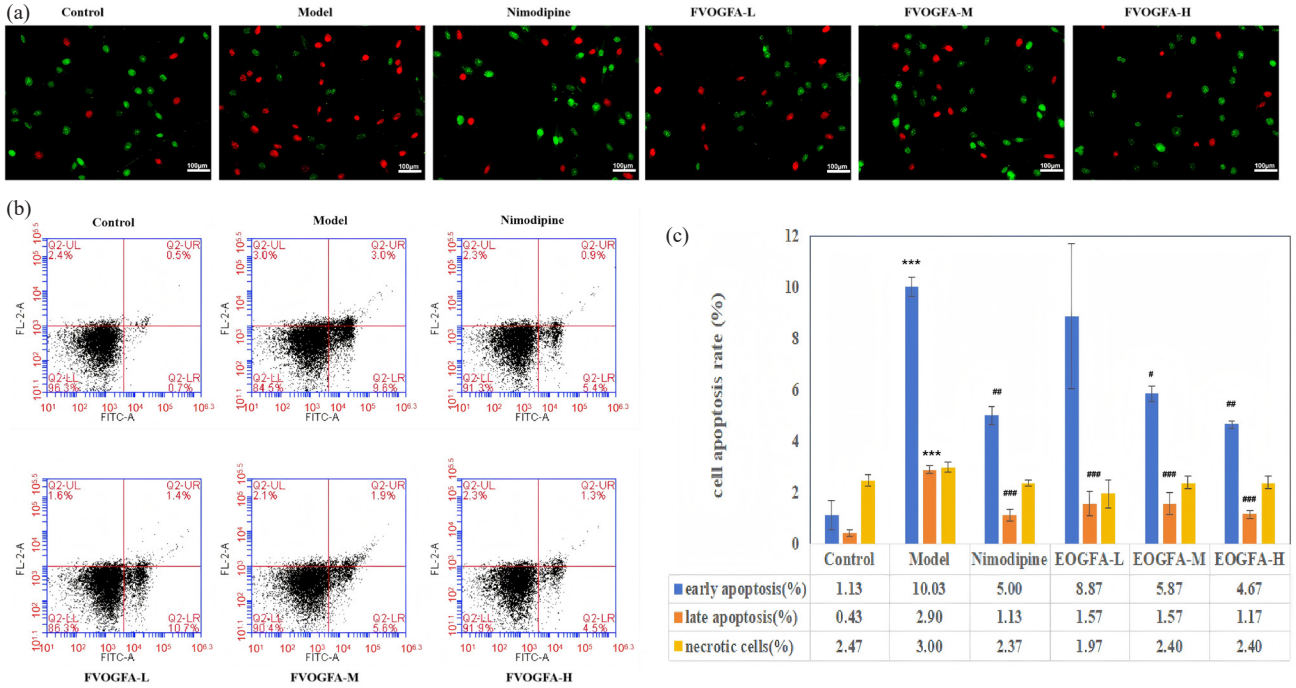

Figure 7. (a) Impact of FVOGFA on apoptosis of PC12 cells subjected to OGD/R treatment (scale bar = 100 μm), (b) flow cytometry instrument to detect early, late and necrosis rate of PC12 cells, (c) the results of apoptosis of PC12 cell in each group. Compared with the control group: $^{*}p < 0.05$, $^{**}p < 0.01$, $^{***}p < 0.001$. Compared with the model group: $^{\#}p < 0.05$, $^{\#\#}p < 0.01$, $^{\#\#\#}p < 0.001$.

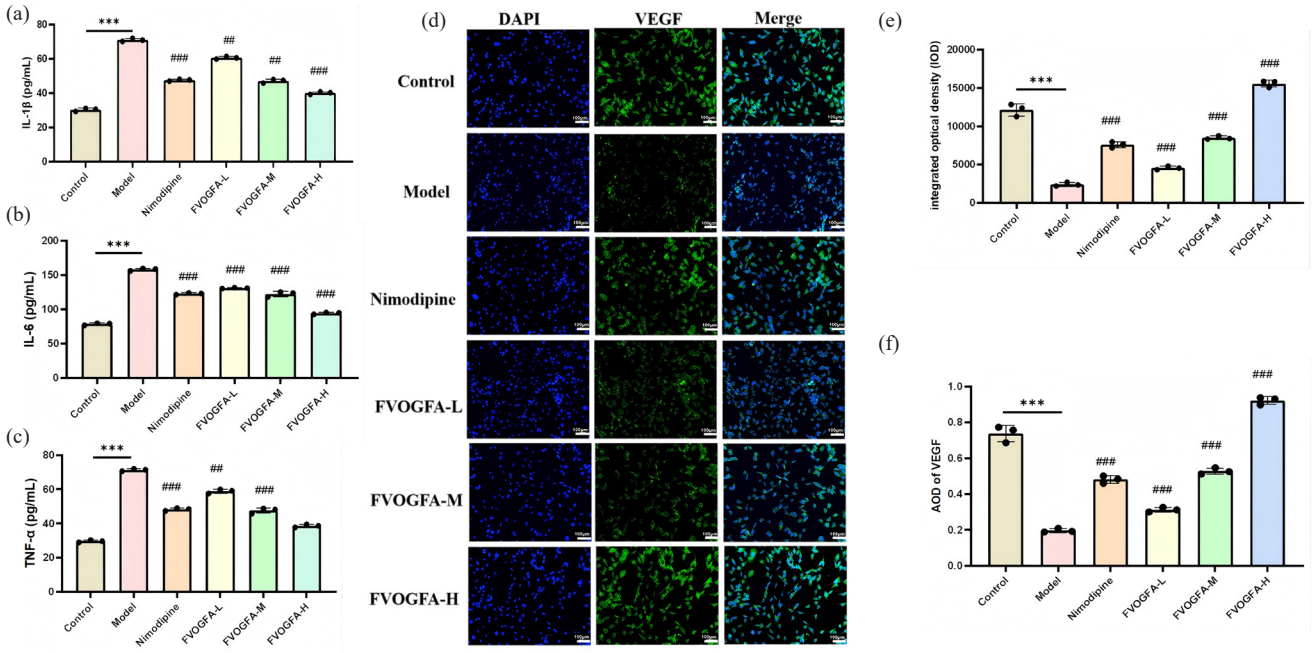

Figure 8. (a-c) FVOGFA alleviates inflammatory damage to PC12 cells induced by OGD/R by inhibiting inflammatory cytokines (IL-1β, IL-6, and TNF-α), (d-f) immunofluorescence staining to detect the expression of VEGF in PC12 cells (scale bar = 100 μm). Compared with the control group: $^{*}p < 0.05$, $^{**}p < 0.01$, $^{***}p < 0.001$. Compared with the model group: $^{\#}p < 0.05$, $^{\#\#}p < 0.01$, $^{\#\#\#}p < 0.001$.

3.9. FVOGFA-mLP significantly improves neurological behavior and reduces brain infarct volume in rats, besides alleviating cortical cell damage

Behavioral scores and brain infarct volumes confirm the therapeutic efficacy of FVOGFA-mLP in OGD/R-induced brain injury. As shown in Figure 9(a), the control and sham groups had a behavioral score of 0, while the model group scored 3.21, indicating a significant difference ($p < 0.01$). Post-modeling symptoms, including the inability to walk, hemiplegia, counterclockwise tail-chasing, and lethargy, confirmed successful induction of brain injury. All treatment groups exhibited lower behavioral scores compared to the model group, with significant improvements in all but the low-dose FVOGFA-mLP group ($p < 0.01$). The medium- and high-dose FVOGFA-mLP groups showed the most substantial therapeutic effects.

Histological analysis further supports the neuroprotective benefits of FVOGFA-mLP. As shown in Figures 9(b) and 9(c), the model group exhibited a significantly higher percentage of brain infarct volume compared to the control group, validating the success of the model. All

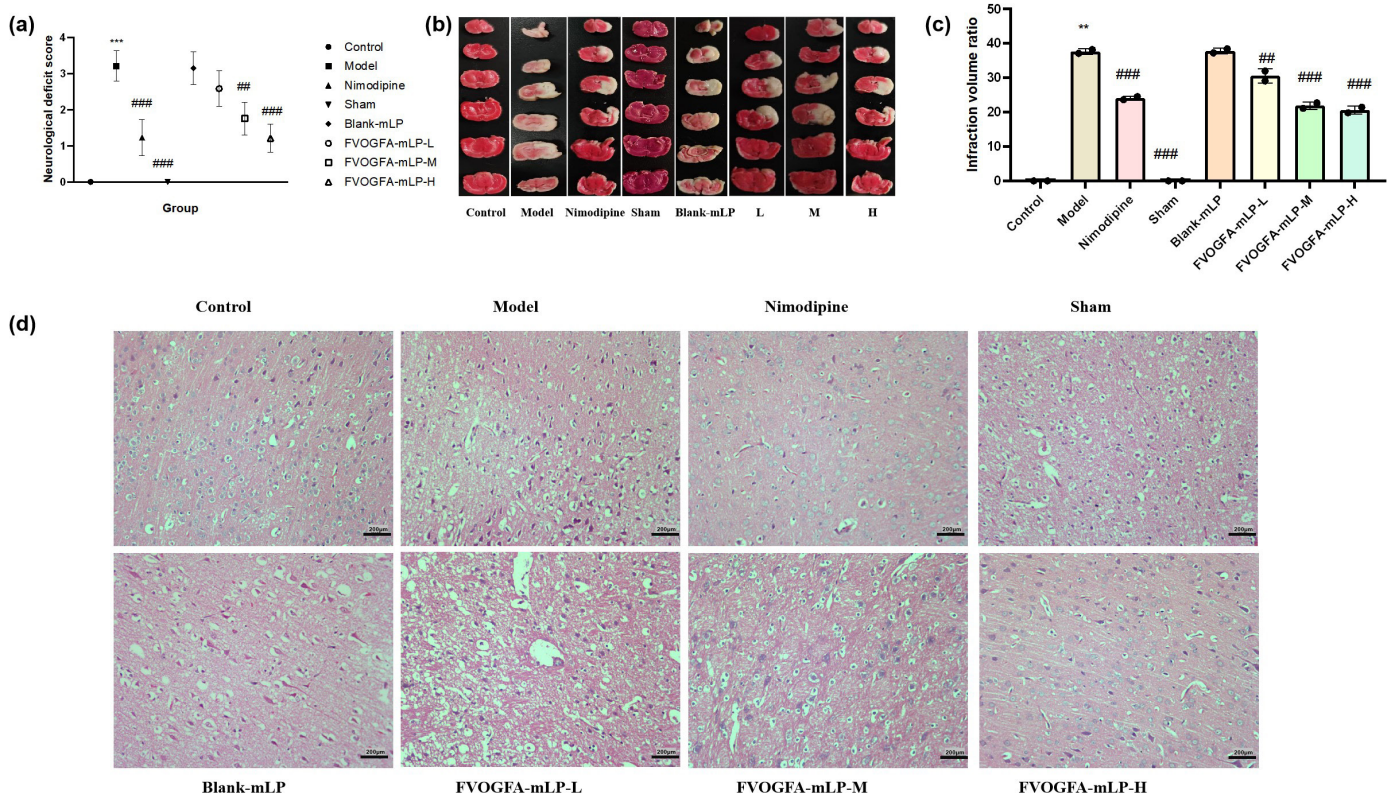

Figure 9. (a) Neurological deficit score of different groups. Effect of FVOGFA-mLP on cerebral infarct area and cerebral ischemia volume ration of MCAO rats, (b) the results of the TTC staining, (c) the infarction rate in different groups. (d) The results of histopathological studies (H&E staining, 200×) on MCAO rats in each group (scale bar = 200 μm). Compared with control group: $^{*}p < 0.05$, $^{**}p < 0.01$, $^{***}p < 0.001$. Compared with the model group: $^{\#}p < 0.05$, $^{\#\#}p < 0.01$, $^{\#\#\#}p < 0.001$.

treatment groups showed a reduction in infarct volume, with significant improvements in all but the blank-mLP group ($p < 0.05$), suggesting that FVOGFA-mLP enhances neurological recovery.

HE staining results (Figure 9d) revealed that high-dose FVOGFA-mLP effectively reduced neuronal necrosis. In the control and sham groups, cortical cells displayed normal morphology with no signs of degeneration, necrosis, inflammation, or gliosis. In contrast, the model and blank-mLP groups showed extensive neuronal necrosis in the marginal zone. The low- and medium-dose FVOGFA-mLP groups exhibited moderate necrosis, while the high-dose FVOGFA-mLP and nimodipine groups showed minimal necrosis, highlighting the superior therapeutic effect of high-dose FVOGFA-mLP.

3.10. FVOGFA-mLP significantly reduces inflammatory cytokine levels, increases VEGF expression, promotes angiogenesis, and ameliorates ischemic brain injury in the cortical area of MCAO rats

FVOGFA-mLP exhibits strong anti-inflammatory effects in the cortical area of MCAO rats (Figures 10a-c). In the model group, levels of inflammatory cytokines TNF-α, IL-6, and IL-1β were significantly elevated ($p < 0.01$) compared to the control group, indicating severe brain inflammation. In contrast, the nimodipine group and all FVOGFA-mLP-treated groups showed significantly reduced levels of these cytokines ($p < 0.01$), with the FVOGFA-mLP-M group displaying a more pronounced reduction than the other dosage groups.

Additionally, FVOGFA-mLP promotes angiogenesis and increases VEGF expression in the cortical area (Figures 10d-f). VEGF expression, significantly reduced in the model group ($p < 0.01$), was restored in all FVOGFA-mLP and nimodipine groups ($p < 0.01$), with the FVOGFA-mLP-M and FVOGFA-mLP-L groups exhibiting slightly higher VEGF expression than the FVOGFA-mLP-H group. $CD31^{+}$ and $Ki67^{+}$ immunofluorescence staining revealed significant increases in angiogenic markers in all treatment groups compared to the model group ($p < 0.01$), confirming the pro-angiogenic effects of FVOGFA-mLP (Figure 11a-c).

At the molecular level, VEGF mRNA expression was significantly reduced in the model group but was restored in all treatment groups ($p < 0.01$), with the FVOGFA-mLP-M group showing no significant difference from the nimodipine group. HIF-1a mRNA, elevated in the model group, was significantly reduced in all FVOGFA-mLP-treated groups, with the highest reduction in the FVOGFA-mLP-H group (Figures 12a-c). Western blot analysis further demonstrated that FVOGFA-mLP significantly reduced the expression of inflammatory and signaling proteins, including TNF-α, SRC, PIK3CA, and MAPK8, with dose-dependent reductions in TNF-α and PIK3CA (Figures 12d-h).

3.11. mPEG-PLA-modified nanoliposomes significantly enhance drug brain-targeting and BBB translocation in both in vitro *and* in vivo *experiments*

mPEG-PLA-modified nanoliposomes demonstrate superior drug delivery through the BBB (Figure 13a). In *in vitro* experiments, the cumulative transport rate of the five active components of VOGFA increased over time for all solutions. However, the mPEG-PLA liposomes showed the highest translocation efficiency across the BBB, while the PBS solution exhibited the lowest rate. These findings indicate that mPEG-PLA-modified nanoliposomes significantly enhance brain-targeting capabilities by efficiently delivering active VOGFA components through the *in vitro* BBB model.

In vivo, mPEG-PLA nanoliposomes further enhance brain-targeting drug delivery (Figure 13b). IVIS imaging in mice revealed no brain fluorescence in the control group, while fluorescence signals appeared rapidly in the nasal and oral regions within 10 to 30 mins after intranasal administration in the Cy7+FVOGFA, Cy7+FVOGFA-mLP, and CIRI model+Cy7+FVOGFA-mLP groups. Fluorescence progressively accumulated in the brain from 30 to 120 mins, with the Cy7+FVOGFA-mLP and CIRI model+Cy7+FVOGFA-mLP groups displaying significantly stronger signals than the Cy7+FVOGFA group. By 360 mins, the Cy7+FVOGFA group had nearly lost all brain fluorescence, while the mPEG-PLA-modified nanoliposome groups maintained strong distribution.

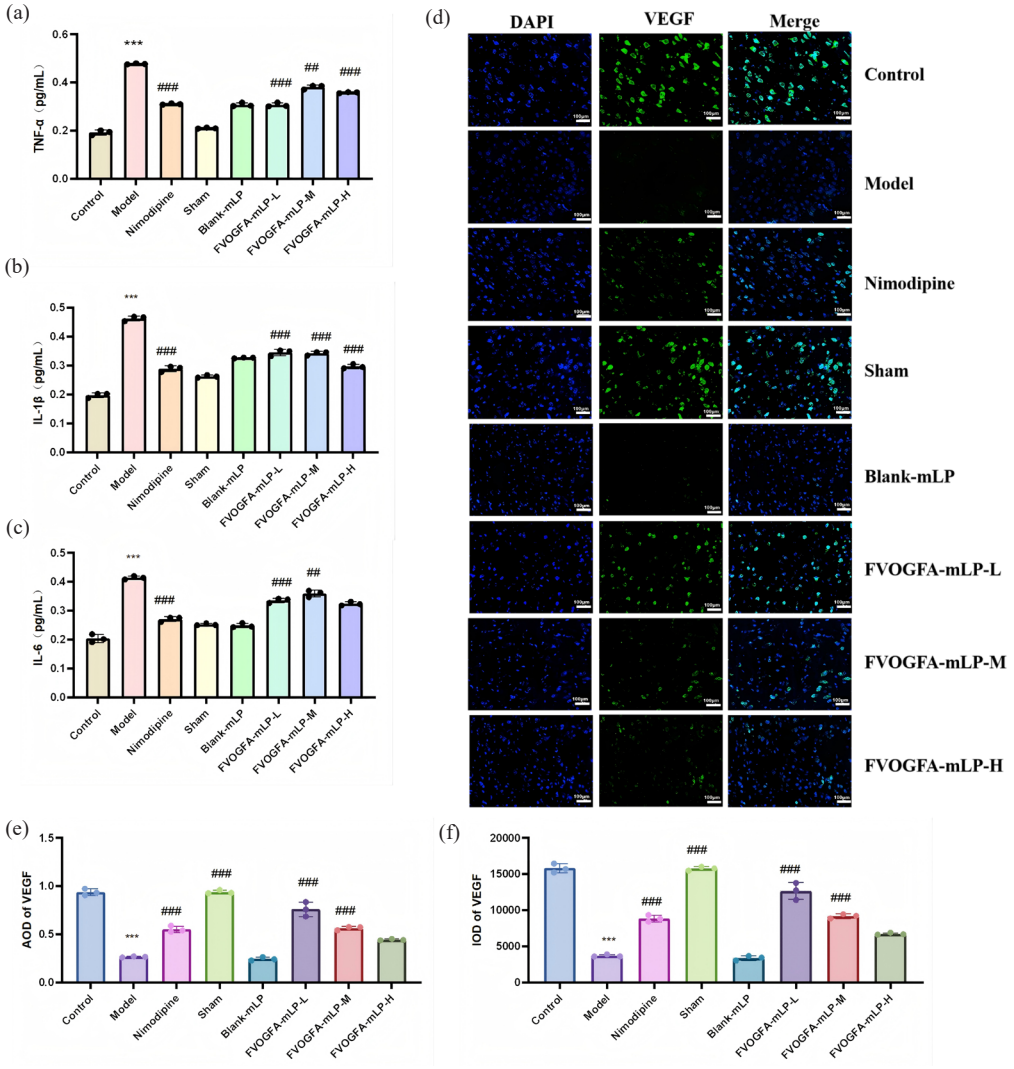

Figure 10. (a-c) The inflammatory cytokines expression and statistics of IL-1β, IL-6, and TNF-α in the ischemic cerebral cortex of different groups (n = 3). (d) The immunofluorescence staining of VEGF in ischemic cerebral cortex (scale bar = 100 μm), green dye is VEGF, blue is DAPI. (e-f) The expression results of VEGF in different groups. Compared with the control group: $^{*}p < 0.05$, $^{**}p < 0.01$, $^{***}p < 0.001$. Compared with the model group: $^{\#}p < 0.05$, $^{\#\#}p < 0.01$, $^{\#\#\#}p < 0.001$.

Formulating drugs into mPEG-PLA liposomes markedly enhances nasal drug delivery efficiency to the brain. *In vivo*, the mPEG-PLA liposome group exhibited significantly higher brain fluorescence intensity compared to the Cy7-only group. Additionally, in CIRI model mice, the disrupted and transiently opened BBB further promoted the brain-targeting efficiency of mPEG-PLA liposomes, highlighting their potential for enhanced drug delivery to the brain.

Based on our previous GC-MS analysis, five active components were identified in the volatile oil: paeonol (37.20%), eugenol (7.80%), methyl eugenol (4.70%), linalool (23.00%), and anethole (27.30%). Studies indicate that paeonol significantly reduces inflammatory responses and cerebral ischemic inflammation, improving neurological deficits in rats and providing neuroprotection against ischemic brain injury [33]. Linalool has demonstrated anti-inflammatory and antioxidant properties, offering protection in models of glutamate-induced oxidative stress and excitotoxicity, suggesting its potential for treating neurodegenerative diseases [34]. Methyl eugenol can cross the BBB and exert therapeutic effects on brain disorders [35]. Anethole reduces neurological deficits, infarct volume, and cerebral edema, providing protection against ischemic stroke [36]. Eugenol, *via* the olfactory pathway, enhances BDNF levels, modulates brain functions, and improves post-ischemic injury [37].

Intranasal administration delivers drugs to the brain *via* the nasal cavity, offering rapid absorption, ease of use, and efficient brain targeting, which is particularly beneficial for patients with impaired consciousness [38,39]. We selected mPEG-PLA polymers as carriers to create targeted nanoliposomes. The hydrophilic PEG provides excellent biocompatibility and low toxicity, while the hydrophobic PLA ensures biodegradability and non-toxic metabolites [40,41]. These mPEG-PLA block copolymers enable both passive and active targeted drug delivery, facilitating efficient transport to brain target sites [42]. Their ability to be transported across the olfactory mucosa makes them ideal for treating brain diseases [43,44]. FVOGFA-mLP, optimized for brain-targeting, exhibited strong sustained-release performance and stability. The ethanol injection method produced nanoliposomes with higher encapsulation efficiency and a clear solution, while the thin-film dispersion method resulted in flocculation and lower encapsulation rates. The sustained-release properties of FVOGFA-mLP are due to mPEG-PLA's structure, where the hydrophilic PEG layer and hydrophobic PLA core create a stable carrier for delayed drug release. Future studies could enhance sustained release by optimizing the mPEG-PLA ratio and nanoliposome structure. Stability testing showed that FVOGFA-mLP performed well at 4°C in the dark, but stability decreased at 25°C, highlighting the need for improved storage conditions to maintain stability across different temperatures.

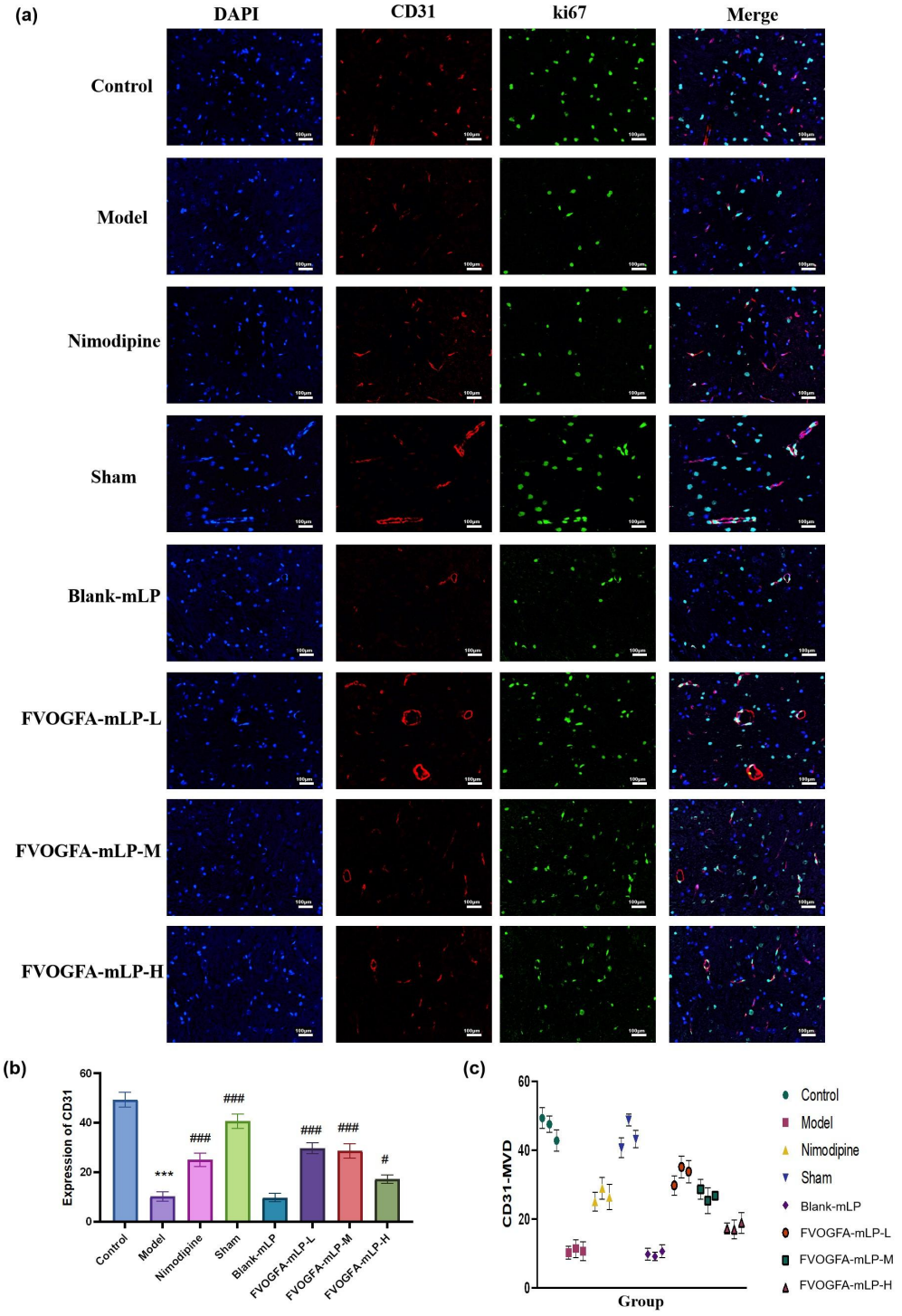

Figure 11. (a) The immunofluorescence staining of $CD31^{+}$/$Ki67^{+}$ in the ischemic cerebral cortex (scale bar = 100 μm). The red dye is $CD31^{+}$, the green dye is $Ki67^{+}$, and the blue is DAPI. (b) The expression of $CD31^{+}$ in the ischemic cerebral cortex, and (c) the expression of $Ki67^{+}$ in the ischemic cerebral cortex. Compared with the control group: $^{*}p < 0.05$, $^{**}p < 0.01$, $^{***}p < 0.001$. Compared with the model group: $^{\#}p < 0.05$, $^{\#\#}p < 0.01$, $^{\#\#\#}p < 0.001$.

The efficacy of FVOGFA-mLP against CIRI primarily targets endothelial cells, which play a key role in BBB disruption, vascular dysfunction, inflammation, platelet aggregation, and coagulation abnormalities, all of which worsen brain tissue damage. Endothelial cells are also critical for neovascularization, a vital process for vascular remodeling following cerebral ischemia [45,46]. Research shows that microvascular formation begins in the infarct core and surrounding areas 4-7 days post-ischemia, guided by VEGF and laminin/B1-integrin signaling [47]. These new vessels express extracellular signals that promote neural stem/progenitor cell proliferation and differentiation, supplying oxygen, nutrients, and soluble factors to the infarct area [48]. In this study, the protective effect of FVOGFA-mLP against cerebral ischemic injury was systematically evaluated by *in vitro* and *in vivo* experiments. The *in vitro* results showed that FVOGFA could significantly improve the survival rate of PC12 cells in the OGD/R model, promote cell migration, reduce cell apoptosis, and alleviate inflammatory injury by inhibiting inflammatory factors (such as IL-1β, IL-6 and TNF-α) and increasing VEGF expression. In the *in vivo* experiment, FVOGFA-mLP significantly improved the neurobehavioral scores of MCAO rats, reduced cerebral infarct volume, and alleviated

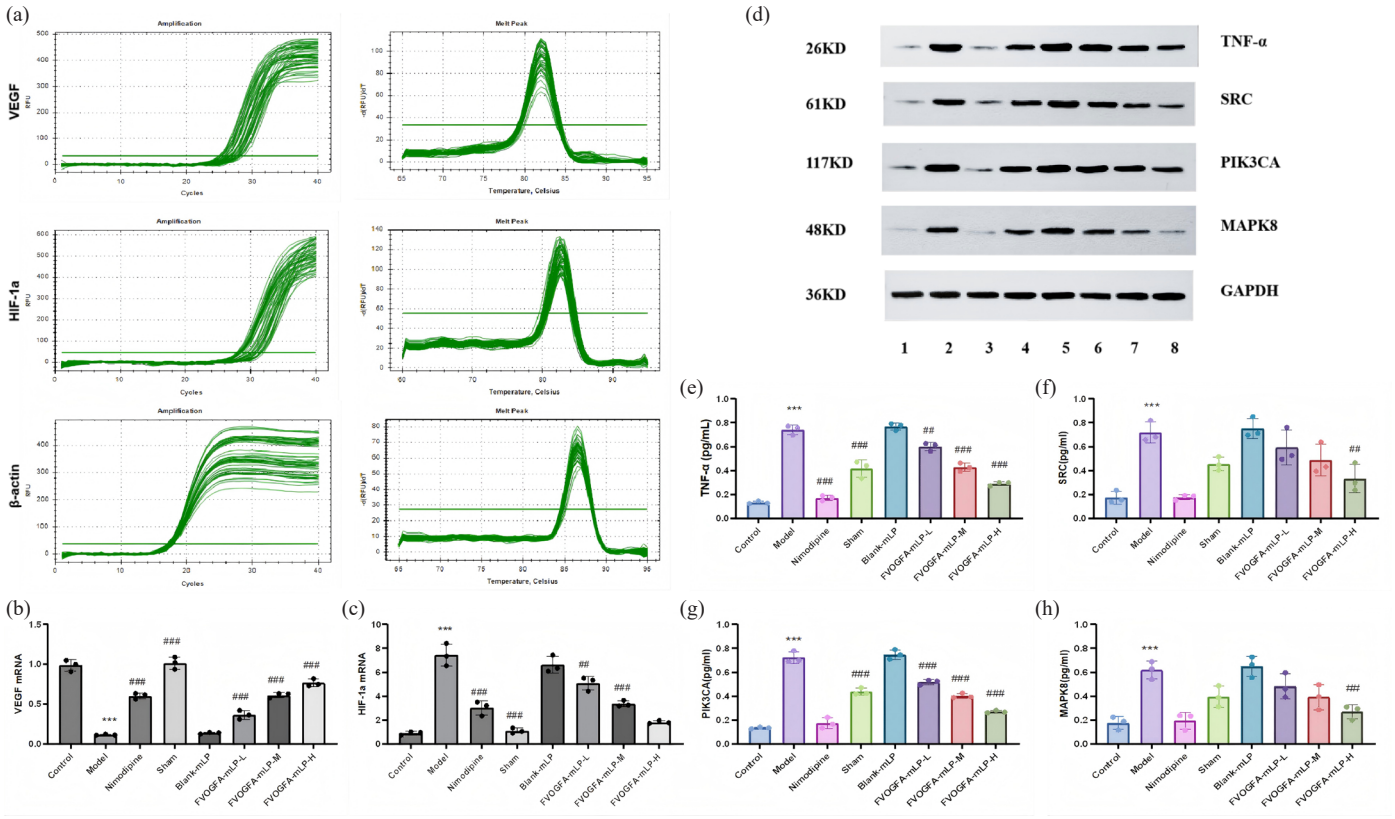

Figure 12. (a) Real-time amplification curves of VEGF, HIF-1a, and β-actin and dissolution curves of amplified products in each group, (b-c) the expression VEGF mRNA and HIF-1a mRNA in each group, (d) the protein expression and statistics of (e) TNF-α, (f) SRC, (g) PIK3CA, and (h) MAPK8 in the ischemic cerebral cortex of different groups (n = 3). Compared with the control group: $^{*}p < 0.05$, $^{**}p < 0.01$, $^{***}p < 0.001$. Compared with the model group: $^{\#}p < 0.05$, $^{\#\#}p < 0.01$, $^{\#\#\#}p < 0.001$. 1: Control; 2: Model; 3: Nimodipine; 4: Sham; 5: Blank-mLP; 6: FVOGFA-mLP-L; 7: FVOGFA-mLP-M; 8: FVOGFA-mLP-H.

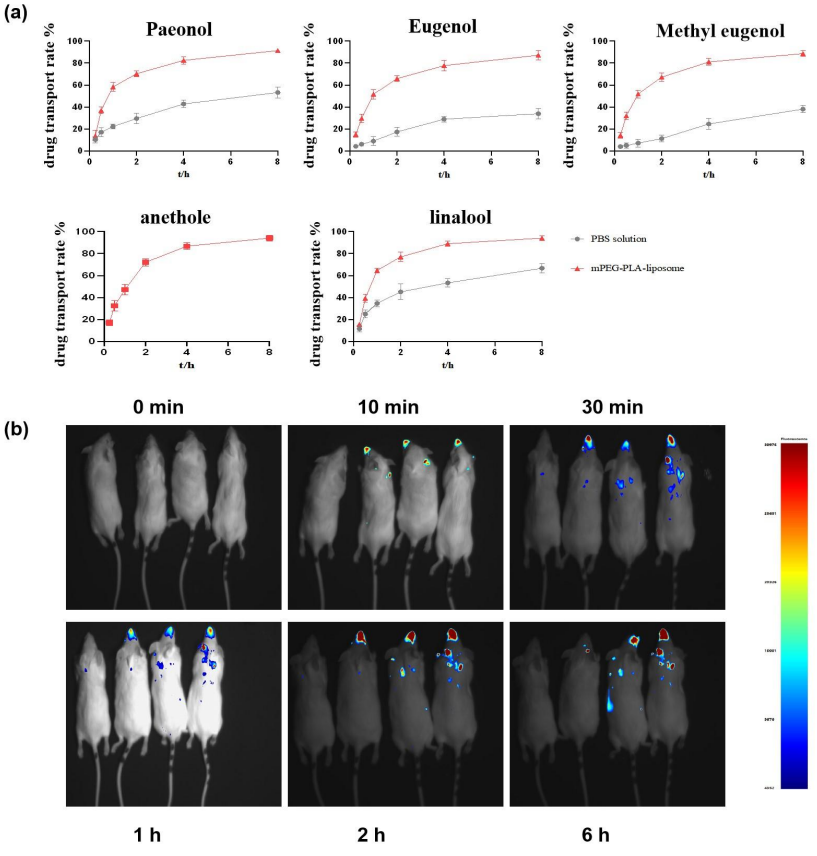

Figure 13. The results of mPEG-PLA-modified nanoliposomes enhance FVOGFA brain-targeting and BBB translocation in both (a) *in vitro* and (b) *in vivo* experiments.

the damage of cortical cells. In addition, FVOGFA-mLP also showed significant anti-inflammatory effects while promoting VEGF expression and angiogenesis *in vivo*. The *in vitro* results were consistent with the *in vivo* results, indicating that FVOGFA had significant neuroprotective and anti-inflammatory effects both *in vitro* and *in vivo*. Notably, the mPEG-PLA-modified nanoliposomes showed excellent BBB penetration and brain targeting *in vitro* and *in vivo*. *In vitro* experiments showed that mPEG-PLA liposomes could significantly improve the BBB transport efficiency of VOGFA active components. *In vivo* experiments further confirmed that mPEG-PLA liposomes could rapidly and continuously accumulate in the brain after intranasal administration, especially in the MCAO model, and the transient opening of the BBB further enhanced its brain targeting efficiency. This finding provides an important experimental basis for the use of FVOGFA-mLP in the treatment of CIRI.

Intranasal administration of FVOGFA-mLP demonstrated the advantage of direct brain delivery, bypassing systemic circulation and enhancing bioavailability. Cy7, a fluorescent probe with excitation and emission wavelengths of 750 nm and 840 nm, can penetrate tissues and cells, making it ideal for tracking drug delivery *in vivo*. In MCAO mice, Cy7-FVOGFA-mLP exhibited stronger and longer-lasting fluorescence compared to Cy7-FVOGFA-mLP alone, likely due to TNF-α and IL-6-induced vascular damage and BBB disruption [49]. These cytokines also activate microglia, transforming them into subtypes that further compromise BBB integrity, allowing more Cy7-FVOGFA-mLP to enter the brain.

HIF-1 is a key transcription factor that regulates cellular adaptation to hypoxia by activating target genes to maintain homeostasis. Comprising α and β subunits, the activity of the α subunit determines the overall function of HIF-1[50]. Research shows that HIF-1α plays a critical role in promoting neural stem cell (NSC) proliferation and differentiation following focal cerebral ischemia in rats [51]. Under hypoxic conditions, HIF-1 regulates VEGF, which is crucial for neurogenesis and angiogenesis, and has neuroprotective effects [52]. Both neurons and astrocytes have VEGF receptors, and neurons can also synthesize VEGF [53]. Ischemic-hypoxic brain injury activates HIF-1α, which induces VEGF overexpression, promoting endothelial cell proliferation and migration, enhancing neovascularization, and protecting endothelial cells from apoptosis, thus reducing ischemic brain damage. Additionally, VEGF inhibits neuronal apoptosis, providing further neuroprotection [54].

Despite the broad application potential of mPEG-PLA-modified nanoliposomes as a brain-targeted drug delivery system, there are still some shortcomings and limitations in practical applications. These issues mainly include the following aspects: First, the issues of biocompatibility and toxicity cannot be overlooked. While PLA exhibits good biocompatibility and low toxicity, potential toxic reactions may still be observed long-term. Therefore, further clinical evaluation of its safety is particularly important. Secondly, there are challenges related to drug release control. The drug release rate of FVOGFA-mLP can be somewhat adjusted by altering the length of the PLA chains; however, ensuring precise control of the release speed and uniform distribution in practical applications remains a complex task. More research is needed to optimize the release mechanism. Furthermore, although the goal of FVOGFA-mLP is to achieve brain targeting, these liposomes may interact with non-target tissues, leading to reduced targeting efficiency. Thus, optimizing the surface properties of liposomes is a key step in enhancing their brain-targeting capability. Finally, the issue of stability cannot be ignored. The stability of liposomes directly affects their drug delivery efficacy, and the stability of FVOGFA-mLP in blood circulation and its ability to cross the BBB still requires further investigation to ensure their effectiveness in clinical applications. Overall, these issues represent the main challenges faced in current research, necessitating effective optimization and improvement in material selection [55], drug design [56], and clinical application [57]. This process requires not only further foundational research support but also interdisciplinary collaboration to advance this field.

In summary, FVOGFA-mLP presents a promising therapeutic strategy for addressing ischemic-reperfusion brain injury. Through its multi-faceted mechanism, including the regulation of HIF-1α and VEGF expression, the reduction of inflammation, and the enhancement of endothelial cell function, FVOGFA-mLP supports neuroprotection, promotes neovascularization and aids in the recovery of brain function. The optimized delivery system, particularly *via* intranasal administration, ensures efficient brain targeting and sustained drug release, offering significant potential for improving treatment outcomes in cerebral ischemic conditions.

4. Conclusions

This study demonstrates that intranasal administration of mPEG-PLA-modified nanoliposomes loaded with FVOGFA significantly enhances neuroprotection in rats with CIRI. The FVOGFA-mLP formulation exhibits superior encapsulation efficiency, stability, and sustained-release properties, effectively delivering five key active components to the brain. *In vitro* and *in vivo* results confirm that FVOGFA-mLP promotes cell survival and migration, reduces apoptosis, alleviates neurological deficits, and decreases infarct volume, primarily by regulating HIF-1α and VEGF pathways. These findings suggest that FVOGFA-mLP offers a promising brain-targeted therapeutic strategy for ischemic stroke, providing significant potential for clinical translation to improve stroke outcomes.

CRediT authorship contribution statement

Wenyuan Chen: Methodology, Investigation, Writing – original draft. **Linli Jiang and Lei Chen:** Resources, Methodology. **Nana Dong, Yong Gao, Lan Qin and Yixue Lin:** Animal experiments and Cell experimensts. **Zhigang Ju and Yuxin Pang:** Supervision, Review. **Xiaolan Chen:** Funding acquisition, Supervision, Writing-review & editing.

Declaration of competing interest

The authors declare that they have no known competing financial interests or personal relationships that could have appeared to influence the work reported in this paper.

Declaration of Generative AI and AI-assisted technologies in the writing process

The authors confirm that there was no use of artificial intelligence (AI)-assisted technology for assisting in the writing or editing of the manuscript and no images were manipulated using AI.

Acknowledgment

This research was supported by the National Natural Science Foundation of China (82460777); National Engineering Technology Research Center for Miao Medicine improved ability (QKHZYD [2023]006); Guizhou Province High-level Innovative Talents Project (Qian ke he Platform Talents - GCC[2023]037).

Supplementary data

Supplementary material to this article can be found online at https://dx.doi.org/10.25259/AJC_76_2024.

References

1. Bennett, D.A., Krishnamurthi, R.V., Barker-Collo, S., Forouzanfar, M.H., Naghavi, M., Connor, M., Lawes, C.M., Moran, A.E., Anderson, L.M., Roth, G.A., Mensah, G.A., Ezzati, M., Murray, C.J., Feigin, V.L., 2014. The global burden of ischemic stroke: Findings of the GBD 2010 study. *Global Heart*, **9**, 107-112. https://doi.org/10.1016/j.gheart.2014.01.001
2. Mărgăritescu, O., Mogoantă, L., Pirici, I., Pirici, D., Cernea, D., Mărgăritescu, C., 2009. Histopathological changes in acute ischemic stroke. *Romanian Journal of Morphology and Embryology = Revue Roumaine de Morphologie et Embryologie*, **50**, 327-339.
3. GBD 2016 DALYs and HALE Collaborators., 2017. Global, regional, and national disability-adjusted life-years (DALYs) for 333 diseases and injuries and healthy life expectancy (HALE) for 195 countries and territories, 1990–2016: A systematic

analysis for the global burden of disease study 2016. *The Lancet*, **390**, 1260-1344. https://doi.org/10.1016/S0140-6736(18)32335-3
4. Bhaskar, S., Stanwell, P., Cordato, D., Attia, J., Levi, C., 2018. Reperfusion therapy in acute ischemic stroke: Dawn of a new era? *BMC Neurology*, **18**, 8. https://doi.org/10.1186/s12883-017-1007-y
5. Wu, L., Xiong, X., Wu, X., Ye, Y., Jian, Z., Zhi, Z., Gu, L., 2020. Targeting oxidative stress and inflammation to prevent ischemia-reperfusion injury. *Frontiers in Molecular Neuroscience*, **13**, 28. https://doi.org/10.3389/fnmol.2020.00028
6. Scheldeman, L., Wouters, A., Lemmens, R., 2022. Imaging selection for reperfusion therapy in acute ischemic stroke beyond the conventional time window. *Journal of Neurology*, **269**, 1715-1723. https://doi.org/10.1007/s00415-021-10872-4
7. Zhao, J., Jiang, P., Zhang, W., 2010. Molecular networks for the study of TCM pharmacology. *Briefings in Bioinformatics*, **11**, 417-430. https://doi.org/10.1093/bib/bbp063
8. Mikitsh, J.L., Chacko, A.M., 2014. Pathways for small molecule delivery to the central nervous system across the blood-brain barrier. *Perspectives in Medicinal Chemistry*, **6**, 11-24. https://doi.org/10.4137/PMC.S13384
9. Chang, C.-F., Lai, J.-H., Wu, J.C.-C., Greig, N.H., Becker, R.E., Luo, Y., Chen, Y.-H., Kang, S.-J., Chiang, Y.-H., Chen, K.-Y., 2017. (−)-phenserine inhibits neuronal apoptosis following ischemia/reperfusion injury. *Brain Research*, **1677**, 118-128. https://doi.org/10.1016/j.brainres.2017.09.015
10. Zhang, J., Zhu, L., Tang, Q., 2021. Electroacupuncture with rehabilitation training for limb spasticity reduction in post-stroke patients: A systematic review and meta-analysis. *Topics in Stroke Rehabilitation*, **28**, 340-361. https://doi.org/10.1080/10749357.2020.1812938
11. Schmutz, J.örg, Engelter, S., Peters, N., Schmucki, P., Gelsomino, M., 2023. Hyperbaric oxygen in post-stroke patients: A feasibility study. *Clinical and Translational Neuroscience*, **7**, 41. https://doi.org/10.3390/ctn7040041
12. Convento, S., Russo, C., Zigiotto, L., Bolognini, N., 2016. Transcranial electrical stimulation in post-stroke cognitive Rehabilitation: Where We Are and Where We Are Going. Hogrefe Publishing.
13. Crowe, T.P., Greenlee, M.H.W., Kanthasamy, A.G., Hsu, W.H., 2018. Mechanism of intranasal drug delivery directly to the brain. *Life Sciences*, **195**, 44-52. https://doi.org/10.1016/j.lfs.2017.12.025
14. Yang, K., Chen, H., Li, R., 2005. Protective mechanism of Naoxing nasal spray on ischemic cerebral injury. *Journal of Guangzhou University of Traditional Chinese Medicine*, **22**, 39-41.
15. Wang, J., Zhang, X.H., Xu, X., Zhu, Q., Yao, B., Liang, S., Chen, Z., Wang, Y., He, M.F., Wu, M., 2020. Pro-angiogenic activity of tongnao decoction on HUVECs in vitro and zebrafish in vivo. *Journal of Ethnopharmacology*, **254**, 112737. https://doi.org/10.1016/j.jep.2020.112737
16. Dahiya, S., Dahiya, R.. An overview on nanocarriers for nasal delivery. In: *Nasal Drug Delivery: Formulations, Developments, Challenges, and Solutions*, pp. 141-168.
17. Jia, C.L., Gou, Y., Gao, Y., Pei, X., Jin, X., Li, B.L., Zhang, Z., He, Y., Ji, E.S., Zhao, Y., 2024. Rosmarinic acid liposomes suppress ferroptosis in ischemic brain *via* inhibition of tfR1 in BMECs. *Phytomedicine: International Journal of Phytotherapy and Phytopharmacology*, **132**, 155835. https://doi.org/10.1016/j.phymed.2024.155835
18. Yang, S., Li, Y., Zheng, X., Zheng, X., Lin, Y., Guo, S., Liu, C., 2024. Effects of folate-chicory acid liposome on macrophage polarization and TLR4/NF-κB signaling pathway in ulcerative colitis mouse. *Phytomedicine: International Journal of Phytotherapy and Phytopharmacology*, **128**, 155415. https://doi.org/10.1016/j.phymed.2024.155415
19. Duan, Y., Zhang, B., Chu, L., Tong, H.H., Liu, W., Zhai, G., 2016. Evaluation in vitro and in vivo of curcumin-loaded mPEG-PLA/TPGS mixed micelles for oral administration. *Colloids and surfaces. B, Biointerfaces*, **141**, 345-354. https://doi.org/10.1016/j.colsurfb.2016.01.017
20. Xiang, C.-C., Ji, J.-G., Liu, Y.-H., Lin, H.-H., Hao, S.-L., 2017. Solubilizing and light protecting effect of mPEG-PLA copolymer micelles on DHA. *Journal of Functional Polymers*, **30**, 221-226. https://doi: 10.14133/j.cnki.1008-9357.2017.02.011
21. Zheng, X., Kan, B., Gou, M., Fu, S., Zhang, J., Men, K., Chen, L., Luo, F., Zhao, Y., Zhao, X., Wei, Y., Qian, Z., 2010. Preparation of MPEG-PLA nanoparticle for honokiol delivery in vitro. *International Journal of Pharmaceutics*, **386**, 262-7. https://doi.org/10.1016/j.ijpharm.2009.11.014
22. Hwang, D., Ramsey, J.D., Kabanov, A.V., 2020. Polymeric micelles for the delivery of poorly soluble drugs: From nanoformulation to clinical approval. *Advanced Drug Delivery Reviews*, **156**, 80-118. https://doi.org/10.1016/j.addr.2020.09.009
23. Zheng, S., Löw, K., Wagner, S., Yang, X., von Briesen, H., Zou, S., 2011. Cytotoxicity of triptolide and triptolide loaded polymeric micelles in vitro. *Toxicology in vitro: An International Journal Published in Association with BIBRA*, **25**, 1557-1567. https://doi.org/10.1016/j.tiv.2011.05.020
24. Xu, L., Qiu, Y., Xu, H., Ao, W., Lam, W., Yang, X., 2013. Acute and subacute toxicity studies on triptolide and triptolide-loaded polymeric micelles following intravenous administration in rodents. *Food and Chemical Toxicology: An International Journal Published for the British Industrial Biological Research Association*, **57**, 371-9. https://doi.org/10.1016/j.fct.2013.03.044
25. Jung, M.A., Song, H.K., Jo, K., Lee, A., Hwang, Y.H., Ji, K.Y., Jung, D.H., Cai, M., Lee, J.Y., Pyun, B.J., Kim, T., 2023. Gleditsia sinensis lam. aqueous extract attenuates nasal inflammation in allergic rhinitis by inhibiting MUC5AC production through suppression of the STAT3/STAT6 pathway. *Biomedicine & Pharmacotherapy = Biomedecine & Pharmacotherapie*, **161**, 114482. https://doi.org/10.1016/j.biopha.2023.114482
26. Lin, M., Rongfei, Z., Shule, Y., Zhengfeng, W., Shouxun, Z., Lei, W., Deng, B., Kebebe, D., 2015. Chemical constituents of fructus gleditsiae abnormalis. *J. China Pharm. Univ.*, **46**, 188-93. https://doi: 10.11665/j.issn.1000-5048.20150209
27. Luo, C., Wu, Y., Chen, X., Han, W., Wan, J., Dong, N., Deng, B., Kebebe, D., 2021. Chemical composition, protective effects, and mechanisms of volatile oil from fructus gleditsiae abnormalis with nasal administration against ischemic injury in HFD and MCAO-induced rats. *Evidence-Based Complementary and Alternative Medicine*, **2021**, 8880996. https://doi: 10.1155/2021/8880996
28. Ding, Q., Wang, X.-P., Xu, F., Zhang, M., Fang, R.-Z., Qin, P., Wu, H.-M., 2022. Exploring the anti-inflammatory effect of fructus gleditsia sinensis lam., fructus gleditsiae abnormalis, and gymnocladus chinensis baill. using SPME-GC-MS, network pharmacology, and molecular docking. *Arabian Journal of Chemistry*, **15**, 103859. https://doi.org/10.1016/j.arabjc.2022.103859
29. Dong, N.-N., Chen, X.-L., Deng, B.-L., Xie, S.-C., Hu, J., 2023. Effective constituents of essential oil from Gleditsiae Fructus Abnormalis and anti-cerebral ischemia/reperfusion injury mechanism: based on GC-MS, network pharmacology, and experimental verification. *Zhongguo Zhong yao za zhi= Zhongguo Zhongyao Zazhi= China Journal of Chinese Materia Medica 48*, 1076-1086. https://doi: 10.19540/j.cnki.cjcmm.20221102.703
30. Ghasemi, R., Abdollahi, M., Emamgholi Zadeh, E., Khodabakhshi, K., Badeli, A., Bagheri, H., Hosseinkhani, S., 2018. mPEG-PLA and PLA-PEG-PLA nanoparticles as new carriers for delivery of recombinant human growth hormone (rhGH). *Scientific Reports*, **8**, 9854. https://doi.org/10.1038/s41598-018-28092-8
31. Sasatsu, M., Onishi, H., Machida, Y., 2006. In vitro and in vivo characterization of nanoparticles made of meO-PEG amine/PLA block copolymer and PLA. *International Journal of Pharmaceutics*, **317**, 167-174. https://doi.org/10.1016/j.ijpharm.2006.02.057
32. Balzus, B., Colombo, M., Sahle, F.F., Zoubari, G., Staufenbiel, S., Bodmeier, R., 2016. Comparison of different in vitro release methods used to investigate nanocarriers intended for dermal application. *International Journal of Pharmaceutics*, **513**, 247-254. https://doi.org/10.1016/j.ijpharm.2016.09.033
33. Mohamed, M.Z., Morsy, M.A., Mohamed, H.H., Hafez, H.M., 2020. Paeonol protects against testicular ischaemia-reperfusion injury in rats through inhibition of oxidative stress and inflammation. *Andrologia*, **52**, e13599. https://doi.org/10.1111/and.13599
34. Sabogal-Guáqueta, A.M., Hobbie, F., Keerthi, A., Oun, A., Kortholt, A., Boddeke, E., Dolga, A., 2019. Linalool attenuates oxidative stress and mitochondrial dysfunction mediated by glutamate and NMDA toxicity. *Biomedicine & Pharmacotherapy = Biomedecine & Pharmacotherapie*, **118**, 109295. https://doi.org/10.1016/j.biopha.2019.109295
35. Irie, Y., 2006. Effects of eugenol on the central nervous system: Its possible application to treatment of Alzheimer's disease, depression, and Parkinson's disease. *Current Bioactive Compounds*, **2**, 57-66. https://doi:10.2174/157340721060201005
36. Younis, N.S., Mohamed, M.E., 2023. Anethole pretreatment modulates cerebral ischemia/Reperfusion: The role of JNK, p38, MMP-2 and MMP-9 pathways. *Pharmaceuticals (Basel, Switzerland)*, **16**, 442. https://doi.org/10.3390/ph16030442
37. Razak, A.M., Tan, J.K., Mohd Said, M., Makpol, S., 2023. Modulating effects of zingiberaceae phenolic compounds on neurotrophic factors and their potential as neuroprotectants in brain disorders and age-associated neurodegenerative disorders: A review. *Nutrients*, **15**, 2564. https://doi.org/10.3390/nu15112564
38. Islam, S.U., Shehzad, A., Ahmed, M.B., Lee, Y.S., 2020. Intranasal delivery of nanoformulations: A potential way of treatment for neurological disorders. *Molecules*, **25**, 1929. https://doi: 10.3390/molecules25081929
39. Pandey, V., Gadeval, A., Asati, S., Jain, P., Jain, N., Roy, R.K., Tekade, M., Soni, V., Tekade, R.K.. Formulation strategies for nose-to-brain delivery of therapeutic molecules. In: *Drug delivery systems*, pp. 291-332. https://doi.org/10.1016/B978-0-12-814487-9.00007-7
40. Li, G., Zhao, M., Xu, F., Yang, B., Li, X., Meng, X., Teng, L., Sun, F., Li, Y., 2020. Synthesis and biological application of polylactic acid. *Molecules (Basel, Switzerland)*, **25**, 5023. https://doi.org/10.3390/molecules25215023
41. Mundel, R., Thakur, T., Chatterjee, M., 2022. Emerging uses of PLA–PEG copolymer in cancer drug delivery. *3 Biotech*, **12**, 41. https://doi.org/10.1007/s13205-021-03105-y
42. Vlachopoulos, A., Karlioti, G., Balla, E., Daniilidis, V., Kalamas, T., Stefanidou, M., Bikiaris, N.D., Christodoulou, E., Koumentakou, I., Karavas, E., Bikiaris, D.N., 2022. Poly(Lactic acid)-based microparticles for drug delivery applications: An overview of recent advances. *Pharmaceutics*, **14**, 359. https://doi.org/10.3390/pharmaceutics14020359
43. Wen, R., Zhang, Q., Xu, P., Bai, J., Li, P., Du, S., Lu, Y., 2016. Xingnaojing mPEG2000-PLA modified microemulsion for transnasal delivery: Pharmacokinetic and brain-targeting evaluation. *Drug Development and Industrial Pharmacy*, **42**, 926-935. https://doi.org/10.3109/03639045.2015.1091471
44. Rabiee, N., Ahmadi, S., Afshari, R., Khalaji, S., Rabiee, M., Bagherzadeh, M., Fatahi, Y., Dinarvand, R., Tahriri, M., Tayebi, L., Hamblin, M.R., Webster, T.J., 2021. Polymeric nanoparticles for nasal drug delivery to the brain: Relevance to alzheimer's disease. *Advanced Therapeutics*, **4**. 2000076. https://doi.org/10.1002/adtp.202000076
45. Lapi, D., Colantuoni, A., 2015. Remodeling of cerebral microcirculation after ischemia-reperfusion. *Journal of Vascular Research*, **52**, 22-31. https://doi.org/10.1159/000381096
46. Hu, X., De Silva, T.M., Chen, J., Faraci, F.M., 2017. Cerebral vascular disease and neurovascular injury in ischemic stroke. *Circulation Research*, **120**, 449-471. https://doi.org/10.1161/CIRCRESAHA.116.308427
47. Kanazawa, M., Takahashi, T., Ishikawa, M., Onodera, O., Shimohata, T., Del Zoppo, G.J., 2019. Angiogenesis in the ischemic core: A potential treatment target? *Journal of Cerebral Blood Flow and Metabolism: Official Journal of the International Society of Cerebral Blood Flow and Metabolism*, **39**, 753-769. https://doi.org/10.1177/0271678X19834158
48. In Park, K., Hack, M.A., Ourednik, J., Yandava, B., Flax, J.D., Stieg, P.E., Gullans, S., Jensen, F.E., Sidman, R.L., Ourednik, V., Snyder, E.Y., 2006. Acute injury directs the migration, proliferation, and differentiation of solid organ stem cells:

Evidence from the effect of hypoxia–ischemia in the CNS on clonal “reporter” neural stem cells. *Experimental Neurology*, **199**, 156-178. https://doi.org/10.1016/j.expneurol.2006.04.002
49. Chen, A.-Q., Fang, Z., Chen, X.-L., Yang, S., Zhou, Y.-F., Mao, L., Xia, Y.-P., Jin, H.-J., Li, Y.-N., You, M.-F., Wang, X.-X., Lei, H., He, Q.-W., Hu, B., 2019. Microglia-derived TNF-α mediates endothelial necroptosis aggravating blood brain–barrier disruption after ischemic stroke. *Cell Death & Disease*, **10**, 487. https://doi.org/10.1038/s41419-019-1716-9
50. Lee, J.-W., Bae, S.-H., Jeong, J.-W., Kim, S.-H., Kim, K.-W., 2004. Hypoxia-inducible factor (HIF-1)α: Its protein stability and biological functions. *Experimental & Molecular Medicine*, **36**, 1-12. https://doi.org/10.1038/emm.2004.1
51. Qi, C., Zhang, J., Chen, X., Wan, J., Wang, J., Zhang, P., Y Liu., 2017, Hypoxia stimulates neural stem cell proliferation by increasing HIF-1α expression and activating Wnt/β-catenin signaling. *Cellular and Molecular Biology (Noisy-le-Grand, France)*, **63**, 12.
52. Lee, J.C., Tae, H.J., Kim, I.H., Cho, J.H., Lee, T.K., Park, J.H., Ahn, J.H., Choi, S.Y., Bai, H.C., Shin, B.N., Cho, G.S., Kim, D.W., Kang, I.J., Kwon, Y.G., Kim, Y.M., Won, M.H., Bae, E.J., 2017. Roles of HIF-1α, VEGF, and NF-κB in ischemic preconditioning-mediated neuroprotection of hippocampal CA1 pyramidal neurons against a subsequent transient cerebral ischemia. *Molecular Neurobiology*, **54**, 6984-6998. https://doi.org/10.1007/s12035-016-0219-2
53. Luth, E.S., Hodul, M., Rennich, B.J., Riccio, C., Hofer, J., Markoja, K., Juo, P., 2021. VER/VEGF receptors regulate AMPA receptor surface levels and glutamatergic behavior. *PLoS Genetics*, **17**, e1009375. https://doi.org/10.1371/journal.pgen.1009375
54. Pan, Z., Ma, G., Kong, L., Du, G., 2021. Hypoxia-inducible factor-1: Regulatory mechanisms and drug development in stroke. *Pharmacological Research*, **170**, 105742. https://doi.org/10.1016/j.phrs.2021.105742
55. Wang, Z., Liang, X., Wang, G., Wang, X., Chen, Y., 2023. Emerging bioprinting for wound healing. *Advanced materials (Deerfield Beach, Fla.)*, e2304738. https://doi.org/10.1002/adma.202304738
56. Chen, Z., Zhang, L., Yang, Y., Cheng, W., Tu, L., Wang, Z., Chen, Y., Hu, W., 2024. Photothermal nanozyme-Encapsulating microneedles for synergistic treatment of infected wounds. *Advanced Functional Materials*, **35**, 2417415. https://doi.org/10.1002/adfm.202417415
57. Hu, W., Wang, W., Chen, Z., Chen, Y., Wang, Z., 2024. Engineered exosomes and composite biomaterials for tissue regeneration. *Theranostics*, **14**, 2099-2126. https://doi.org/10.7150/thno.93088